RADC-TR-89-239
Final Technical Report
November 1989

AD-A217 479

RECENT IMPROVEMENTS TO THE ELECTROMAGNETIC SURFACE PATCH CODE

Ohio State University

Edward H. Newman

90 02 05 082

REPORT DOCUMENTATION PAGE

Form Approved
OMB No. 0704-0188

1a. REPORT SECURITY CLASSIFICATION UNCLASSIFIED			1b. RESTRICTIVE MARKINGS N/A		
2a. SECURITY CLASSIFICATION AUTHORITY N/A			3. DISTRIBUTION/AVAILABILITY OF REPORT Approved for public release; Distribution unlimited.		
2b. DECLASSIFICATION/DOWNGRADING SCHEDULE N/A					
4. PERFORMING ORGANIZATION REPORT NUMBER(S) N/A			5. MONITORING ORGANIZATION REPORT NUMBER(S) RADC-TR-89-239		
6a. NAME OF PERFORMING ORGANIZATION Ohio State University		6b. OFFICE SYMBOL (If applicable)	7a. NAME OF MONITORING ORGANIZATION Rome Air Development Center (EEAA)		
6c. ADDRESS (City, State, and ZIP Code) 1320 Kinnear Road Columbus OH 43212			7b. ADDRESS (City, State, and ZIP Code) Hanscom AFB MA 01731-5000		
8a. NAME OF FUNDING/SPONSORING ORGANIZATION Rome Air Development Center		8b. OFFICE SYMBOL (If applicable) EEAA	9. PROCUREMENT INSTRUMENT IDENTIFICATION NUMBER F30602-81-C-0206		
8c. ADDRESS (City, State, and ZIP Code) Hanscom AFB MA 01731-5000			10. SOURCE OF FUNDING NUMBERS		

10. SOURCE OF FUNDING NUMBERS			
PROGRAM ELEMENT NO.	PROJECT NO.	TASK NO	WORK UNIT ACCESSION NO.
61102F	3356	00	P1

11. TITLE (Include Security Classification)

RECENT IMPROVEMENTS TO THE ELECTROMAGNETIC SURFACE PATCH CODE

12. PERSONAL AUTHOR(S)
Edward H. Newman

13a. TYPE OF REPORT Final	13b. TIME COVERED FROM May 87 TO Sep 87	14. DATE OF REPORT (Year, Month, Day) November 1989	15. PAGE COUNT 60

16. SUPPLEMENTARY NOTATION

N/A

17. COSATI CODES			18. SUBJECT TERMS (Continue on reverse if necessary and identify by block number)
FIELD	GROUP	SUB-GROUP	Radar-cross section (RCS)
09	01		Four element dipole array
			ESP code

19. ABSTRACT (Continue on reverse if necessary and identify by block number)

This report describes two improvements to the "Electromagnetic Surface Patch" or ESP code. ESP is a user oriented computer code, based upon the method of moments (MM), for the analysis of thin wires and polygonal plates. The two improvements to ESP are: (1) The ability to compute near zone fields and (2) the ability to analyze thin dielectric plates through the use of a sheet impedance approximation. This report will describe these two modifications and present numerical data validating the accuracy of the code.

20. DISTRIBUTION/AVAILABILITY OF ABSTRACT ☐ UNCLASSIFIED/UNLIMITED ☒ SAME AS RPT. ☐ DTIC USERS	21. ABSTRACT SECURITY CLASSIFICATION UNCLASSIFIED	
22a. NAME OF RESPONSIBLE INDIVIDUAL Jeffrey Herd	22b. TELEPHONE (Include Area Code) (617) 377-4664	22c. OFFICE SYMBOL RADC (EEAA)

DD Form 1473, JUN 86   *Previous editions are obsolete.*

Contents

1

List of Figures

Chapter 1

Introduction

This report will describe two improvements to the "Electromagnetic Surface Patch" or ESP code. ESP is a user oriented computer code, based upon the method of moments (MM) [1], for the analysis of thin wires and polygonal plates. ESP has been distributed to over 100 users in industry, government, and universities.

The latest version, ESP Version III, was released in May 1987 [2]. In brief, ESP Version III can treat geometries consisting of:

1. thin wires with finite or perfect conductivity and lumped loads,

2. perfectly conducting polygonal plates,

3. wire/plate junctions (at least 0.1 λ from a plate edge)

4. plate/plate junctions, including several plates which intersect along a common edge,

5. excitation by either a plane wave or a delta gap voltage generator.

ESP III is capable of computing most of the quantities of engineering interest including:

1. current distributions,

2. input impedance, input admittance, and radiation efficiency,

3. mutual coupling,

4. far zone gain patterns (both polarizations)

5. far zone plane wave scattering patterns (full scattering matrix).

Notice that ESP III can only treat perfectly conducting plates. However, using the sheet impedance approximation we have modified the code so that it can treat electrically thin dielectric plates. The dielectric plates may be lossy. Also ESP III can only compute far zone radiation and scattering patterns. However ESP has now been modified to be able to compute near zone radiation and scattering patterns, including the radial component of the field. By near zone patterns we mean that the field point can be the in near zone of the radiating antenna or scatterer. These two modifications have been incorporated into the ESP code, and will become part of ESP Version IV. All of the numerical data in this report was run with this preliminary version of ESP IV. Although it will not be described in this report, ESP has also been modified so that it can efficiently generate data over a wide frequency bandwidth [3].

In this report all fields and currents are time harmonic, with the $e^{j\omega t}$ time dependence suppressed.

Chapter 2

Modifications to ESP

2.1 Near Zone Fields

As mentioned above, previous versions of the ESP code are limited to computing far zone patterns. That is, the field point is at an infinite radius from the radiating or scattering body. However, we have now increased the generality of the ESP code by allowing the field point to be at a finite radius from the body. While in the far zone only the transverse components of the fields are nonzero, in the near zone the nonzero radial component is computed.

Gain and radar cross-section (RCS) at a near zone field point will now be defined so that they are consistent with the usual far zone definitions. We will start with the definition of gain. Thus we consider an antenna excited by a generator and which radiates an electric field, $E(r,\theta,\phi)$, which is a function of the spherical (r,θ,ϕ) coordinates of the field point. Let $E(r,\theta,\phi)$ denote a given polarization of the vector electric field. It is well known that in the far zone (i.e., in the limit as $r \to \infty$) the radial dependence of the field is simply

$$e^{-jkr}/r.$$

For this reason, in the far zone, the electric field is usually written as

$$E(r,\theta,\phi) = \frac{e^{-jkr}}{r} E_F(\theta,\phi), \qquad (2.1)$$

where E_F is referred to as the far zone electric field and is independent of r. From Equation 2.1, the far zone electric field is related to the actual

3

electric field by

$$E_F(\theta, \phi) = \lim_{r \to \infty} r e^{jkr} E(r, \theta, \phi). \tag{2.2}$$

The far zone zone directivity of an antenna in a given direction is the ratio of the radiation intensity in that direction to the average radiation intensity of the antenna. The far zone gain is the product of the directivity and the radiation efficiency. The radiation efficiency is the ratio of the total power radiated by the antenna to the total power input to the antenna. The far zone gain is simply related to the far zone electric field by

$$G_F(\theta, \phi) = \frac{|E_F(\theta, \phi)|^2}{30 P_{in}}, \tag{2.3}$$

where P_{in} is the total power input to the antenna.

Corresponding to Equation 2.2, we can define a near zone field as

$$E_N(r, \theta, \phi) = r e^{jkr} E(r, \theta, \phi). \tag{2.4}$$

Note that E_N is a function of r as well as θ and ϕ, since for finite r, the radial dependence of E is not exactly e^{-jkr}/r. However, as r gets large, E_N will become independent of r and approach E_F. We now define the near zone gain as

$$G_N(r, \theta, \phi) = \frac{|E_N(r, \theta, \phi)|^2}{30 P_{in}}, \tag{2.5}$$

The advantage of the above definition of near zone gain is that it allows G_N to be directly compared to G_F without the need for a radial dependent scale factor. Also, as r gets large G_N will approach G_F.

If in Equation 2.3 we insert the $\hat{\theta}$ component of the electric field, then we obtain the $\hat{\theta}$ polarized gain, If we insert the $\hat{\phi}$ polarization, then we get the $\hat{\phi}$ polarized gain. Similarly, the near zone gain of Equation 2.5 has $\hat{r}$, $\hat{\theta}$, and $\hat{\phi}$ components.

Next consider the definition of RCS in the near and far zone. We will still denote $E(r, \theta, \phi)$ as the radiated field of the target, but we will now assume that the target currents were induced by a plane wave of magnitude E_i incident from the direction (θ_i, ϕ_i). The far zone bistatic echo area or RCS is given by

$$\sigma_F(\theta, \phi) = 4\pi \frac{|E_F(\theta, \phi)|^2}{|E_i|^2}. \tag{2.6}$$

4

If $(\theta, \phi) = (\theta_i, \phi_i)$, then σ_F is referred to as the backscatter RCS. If $(\theta, \phi) = (\pi - \theta_i, \pi + \phi_i)$, then σ_F is referred to as the forward RCS. Similarly we will define the near zone bistatic RCS as

$$\sigma_N(r, \theta, \phi) = 4\pi \frac{|E_N(r, \theta, \phi)|^2}{|E_i|^2}. \qquad (2.7)$$

σ_F has four components, corresponding to the possible polarizations of the incident and far zone scattered plane waves. These are:

$\hat{\theta}$ incident and $\hat{\theta}$ scattered

$\hat{\phi}$ incident and $\hat{\phi}$ scattered

$\hat{\theta}$ incident and $\hat{\phi}$ scattered

$\hat{\phi}$ incident and $\hat{\theta}$ scattered.

σ_N has the above four components plus

$\hat{\theta}$ incident and $\hat{r}$ scattered

$\hat{\phi}$ incident and $\hat{r}$ scattered

since the near zone scattered field can have a radial component. ESP IV will output the magnitude and phase of the near or far zone gain and RCS. By the phase of the near or far zone gain or RCS, we mean the phase of E_N or E_F, respectively.

The computation of near zone fields will be illustrated with the four element dipole array shown in Figure 2.1. Here we have four $\lambda/2$ dipoles located $\lambda/4$ in front of a perfectly conducting $1.2\lambda \times 0.75\lambda$ reflecting plate. A three view plot of the wire and plate geometry, supplied by the ESP code, is shown in Figure 2.2. Here it can be seen that for the MM solution each dipole is split into 4 equal segments, which results in 3 piecewise sinusoidal modes on each dipole. The plate is modelled by 38 surface patch modes. The dipoles are perfectly conducting with a radius of 0.001 λ. Each dipole is fed by an in phase one volt generator, which in the far zone will produce a beam maximum on the $+x$ axis, that is at $\theta = 90°$ and $\phi = 0$. We will now show that as the radius of the near zone gain patterns for the dipole array increases, the near zone gain patterns approach the far zone gain patterns.
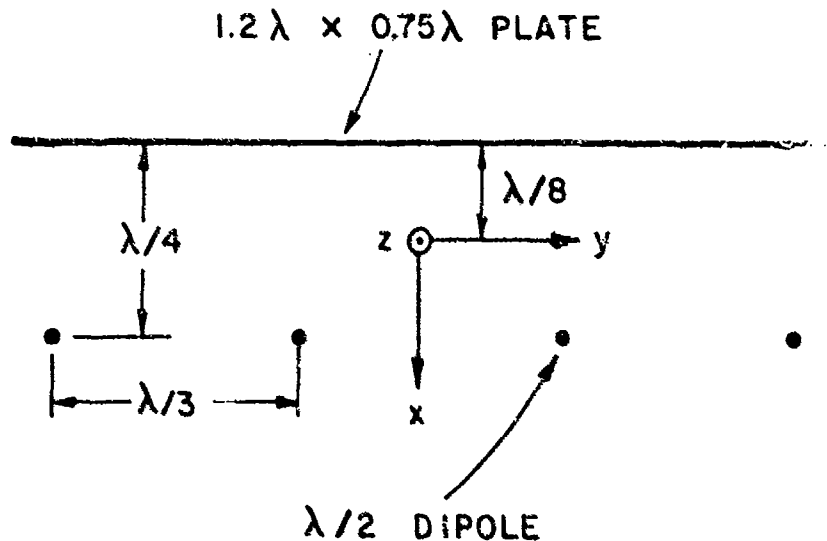
5

Figure 2.1: Top View of four $\lambda/2$ dipoles located $\lambda/4$ in front of a $1.2\lambda \times 0.75\lambda$ reflecting plate.

For the dipole array, Figures 2.3,2.4 show the far zone gain in the azimuth plane $\theta = 90^0$ and in the elevation plane $\phi = 0$. Only the $\hat{\theta}$ polarization is shown, since in these planes there is no $\hat{\phi}$ polarization. By contrast Figures 2.5-2.9 show the $\hat{\theta}$ polarized near zone gain in the azimuth plane and for $r = 0.7, 1, 2, 5$, and 10 λ. Figures 2.10-2.14 and 2.15-2.19 show the $\hat{\theta}$ and $\hat{\phi}$ polarized near zone gain in the elevation plane and for the same r values. Note that all of these pattern plots are supplied by the ESP code.

Comparing Figures 2.3 and 2.5 shows that the near zone azimuth plane pattern at $r = 0.7\lambda$ is considerably different from the far zone pattern. In particular, the peak gain at $r = 0.7\lambda$ is 7.2 dB, as compared to 9.3 dB in the far zone. Also, the beamwidth at $r = 0.7\lambda$ is much wider than the beamwidth in the far zone. There are two main reasons for these differences. First, the uniform phase taper will produce radiation from each dipole which adds in phase at $\theta = 90^0$ and $\phi = 0$ in the far zone zone, but not at $r = 0.7\lambda$. Thus, the peak near zone gain is less than the peak far zone gain. Second, in the near zone the end elements in the dipole array are much closer to the field points near $\phi = \pm 90^0$ than the center elements. This increases the field intensity near $\phi = \pm 90^0$ and thus increases the near

GEOMETRY FOR 4 ELEMENT DIPOLE ARRAY

```
                              12 WIRE MODES
                              38 PLATE MODES
                               0 ATTACH. MODES
    _____               50 TOTAL MODES
                             |SCALE| =  0.440λ
    .    .    .    .         |————|

      Z AXIS VIEW
```
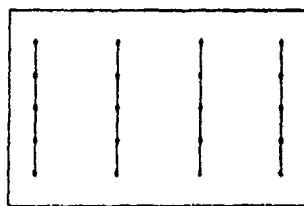
```
   ┌─────────────┐
   │ │ │ │ │ │ │ │           │    │
   │ │ │ │ │ │ │ │           │    │
   │ │ │ │ │ │ │ │           │    │
   └─────────────┘

     X AXIS VIEW              Y AXIS VIEW
```
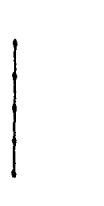
Figure 2.2: A three view sketch of the four element dipole array and reflecting plate of Figure 2.1.

7

zone beamwidth. Comparing Figure 2.3 to Figures 2.5-2.9 shows that as r increases, the near zone azimuth patterns approaches the far zone pattern.

Figures 2.10-2.14 show the $\hat{\theta}$ polarized near zone elevation plane patterns at $r = 0.7, 1, 2, 5,$ and 10 λ. Comparing Figures 2.4 and 2.10 shows that the near zone elevation plane pattern at $r = 0.7\lambda$ is considerably different than the far zone pattern. However, comparing Figure 2.4 to 2.10-2.14 shows that as r increases the near zone elevation plane patterns approach the far zone pattern.

In the far zone the $\hat{r}$ component of all fields is zero, but in the near zone it is not. For the dipole array Figures 2.15-2.19 show the $\hat{r}$ polarized gain in the near zone and for $r = 0.7, 1, 2, 5,$ and 10 λ. Note that as r increases, the level of the $\hat{r}$ polarized gain decreases from -6.4 dB at $r = 0.7\lambda$ to -22.6 dB at $r = 10\lambda$.

Next we will consider the RCS of the dipole array shown in Figures 2.1 and 2.2. For a $\hat{\theta}$ polarized incident and scattered plane wave, Figure 2.20 shows the far zone backscatter RCS pattern in the azimuth plane $\theta = 90^\circ$. Figures 2.21-2.25 show the corresponding near zone RCS patterns for $r = 0.7, 1, 2, 5,$ and 10 λ. Although the RCS is shown in units of dB over a square meter, in this case it is equivalent to dB over a square wavelength, since the computations were made at a frequency of 300 Mhz ($\lambda = 1$ meter). Comparing Figures 2.20 and 2.21 shows that the RCS at $r = 0.7\lambda$ is considerably different from the far zone RCS. However, as r increases, the near zone RCS does approach the far zone RCS.

In summary, the capability to compute near zone fields has been added to the ESP code. Other than numerical integrations, no approximations are involved in the computation of the near zone fields, which are not also made in the computation of the far zone fields. The above data suggests that we have properly modified ESP to compute near zone fields. The main limitations are that if the field point gets too close to the wire/plate geometry, artificial slope discontinuities in the MM expansion modes will cause anomalous behavior in the computed near zone fields. For this reason the field point should not be closer than about a tenth of a wavelength from the wire/plate geometry.

4 ELEMENT DIPOLE ARRAY
FREQUENCY = 300.00 MHZ.
GAIN
POLARIZATION: θ
AZIM. PLANE: θ = 90°   R = ∞
MAXIMUM = 9.300 DB   10 DB/DIV.

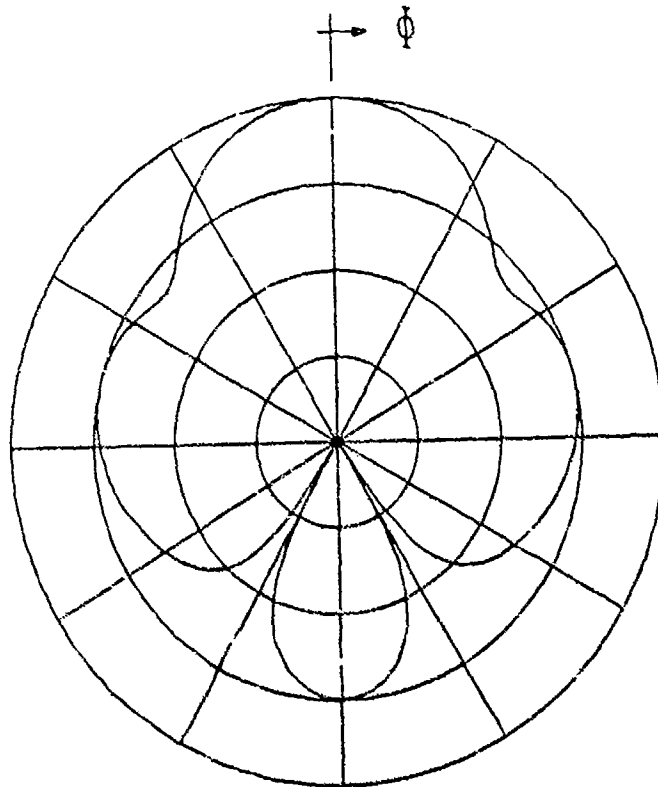Figure 2.3: θ polarized far zone gain for the dipole array in the azimuth plane.

4 ELEMENT DIPOLE ARRAY
FREQUENCY = 300.00 MHZ.
GAIN
POLARIZATION: θ
ELEV. PLANE: ϕ = $0°$ R = ∞
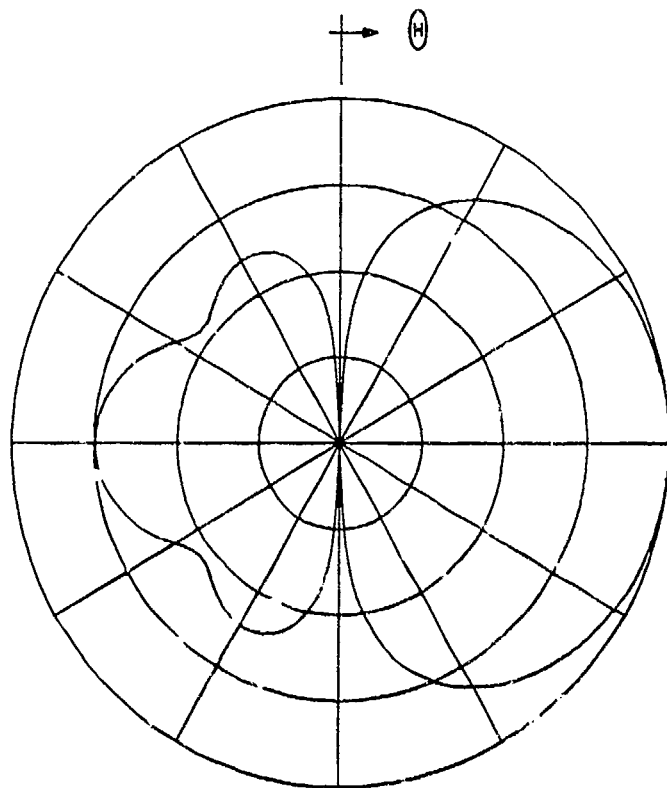MAXIMUM = 9.300 DB   10 DB/DIV.

Figure 2 4: $\hat{\theta}$ polarized far zone gain for the dipole array in the elevation plane.

4 ELEMENT DIPOLE ARRAY
FREQUENCY = 300.00 MHZ.
GAIN
POLARIZATION: Θ
AZIM. PLANE: Θ = 90°   R= 0.700 M
MAXIMUM = 7.200 DB   10 DB/DIV.

Figure 2.5: $\hat{\theta}$ polarized near zone gain at $r = 0.7\lambda$ for the dipole array in the azimuth plane.

4 ELEMENT DIPOLE ARRAY
FREQUENCY = 300.00 MHZ.
GAIN
POLARIZATION: Θ
AZIM. PLANE: Θ = 90° R= 1.000 M
MAXIMUM = 8.300 DB   10 DB/DIV.

Figure 2.6: $\hat{\theta}$ polarized near zone gain at $r = 1\lambda$ for the dipole array in the azimuth plane.

```
4 ELEMENT DIPOLE ARRAY
FREQUENCY =  300.00 MHZ.
GAIN
POLARIZATION:  θ
AZIM. PLANE: θ =  90°   R=  2.000 M
MAXIMUM =  9.100 DB      10 DB/DIV.
```

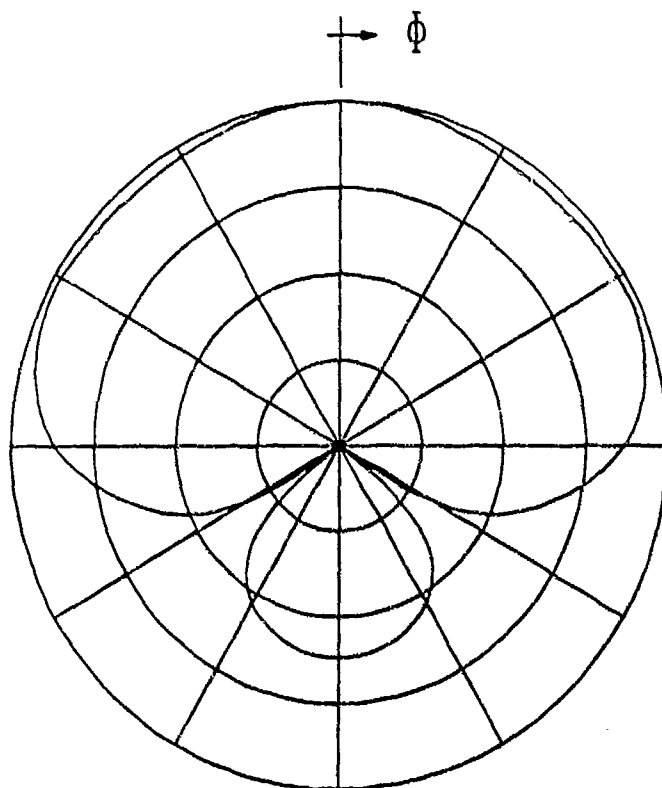Figure 2.7: $\hat{\theta}$ polarized near zone gain at $r = 2\lambda$ for the dipole array in the azimuth plane.

4 ELEMENT DIPOLE ARRAY
FREQUENCY = 300.00 MHZ.
GAIN
POLARIZATION: θ
AZIM. PLANE: θ = 90°   R= 5.000 M
MAXIMUM = 9.300 DB   10 DB/DIV.

Figure 2.8: $\hat{\theta}$ polarized near zone gain at $r = 5\lambda$ for the dipole array in the azimuth plane.

14

4 ELEMENT DIPOLE ARRAY
FREQUENCY = 300.00 MHZ.
GAIN
POLARIZATION: θ
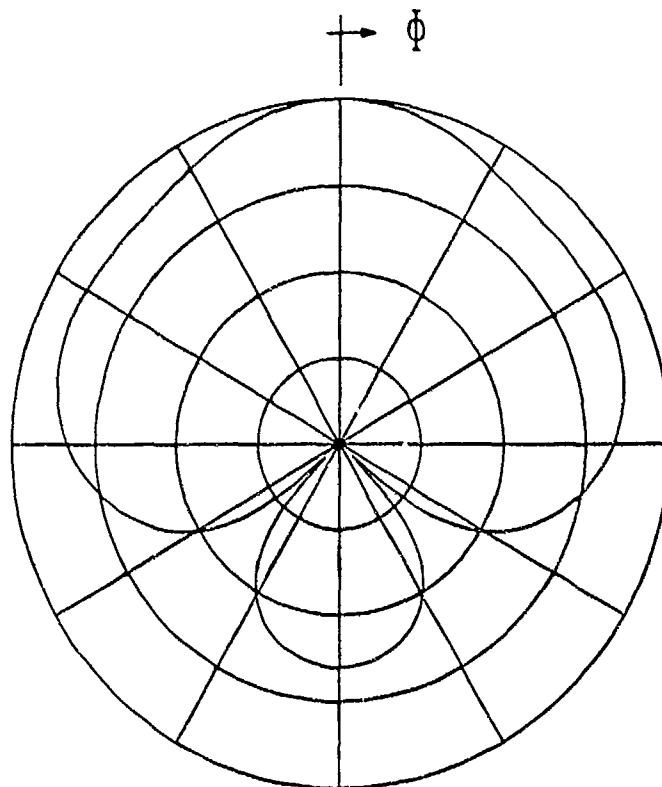AZIM. PLANE: θ = 90° R= 10.000 M
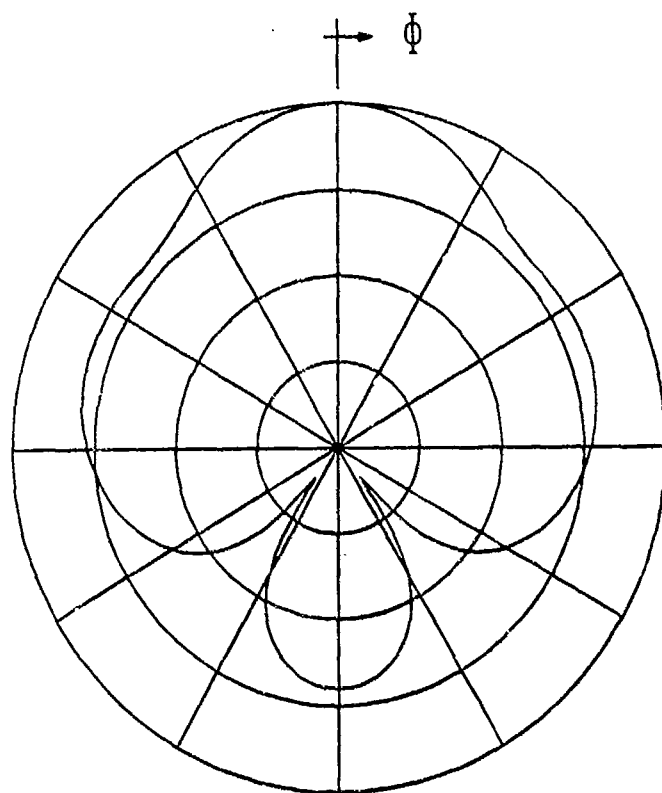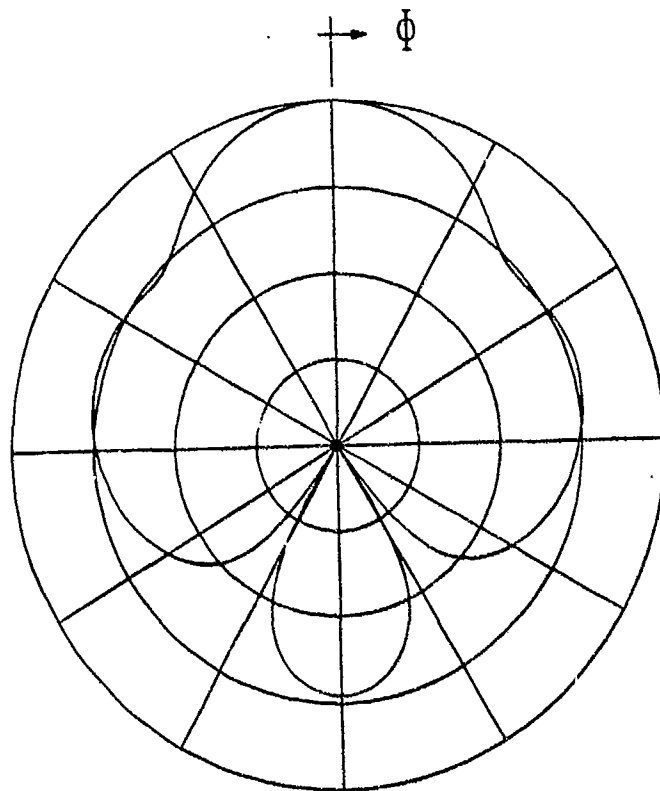MAXIMUM = 9.300 DB 10 DB/DIV.

Figure 2.9: $\hat{\theta}$ polarized near zone gain at $r = 10\lambda$ for the dipole array in the azimuth plane.

4 ELEMENT DIPOLE ARRAY
FREQUENCY = 300.00 MHZ.
GAIN
POLARIZATION: θ
ELEV. PLANE: ϕ = 0° R= 0.700 M
MAXIMUM = 7.200 DB 10 DB/DIV.

Figure 2.10: $\hat{\theta}$ polarized near zone gain at $r = 0.7\lambda$ for the dipole array in the elevation plane.

16

4 ELEMENT DIPOLE ARRAY
FREQUENCY = 300.00 MHZ.
GAIN
POLARIZATION: θ
ELEV. PLANE: ϕ = 0° R= 1.000 M
MAXIMUM = 8.300 DB 10 DB/DIV.

Figure 2.11: $\hat{\theta}$ polarized near zone gain at $r = 1\lambda$ for the dipole array in the elevation plane.

4 ELEMENT DIPOLE ARRAY
FREQUENCY = 300.00 MHZ.
GAIN
POLARIZATION: θ
ELEV. PLANE: φ = 0° R= 2.000 M
MAXIMUM = 9.100 DB 10 DB/DIV.

Figure 2.12: θ polarized near zone gain at $r = 2\lambda$ for the dipole array in the elevation plane.

4 ELEMENT DIPOLE ARRAY
FREQUENCY = 300.00 MHZ.
GAIN
POLARIZATION: θ
ELEV. PLANE: ϕ = 0° R= 5.000 M
MAXIMUM = 9.300 DB 10 DB/DIV.
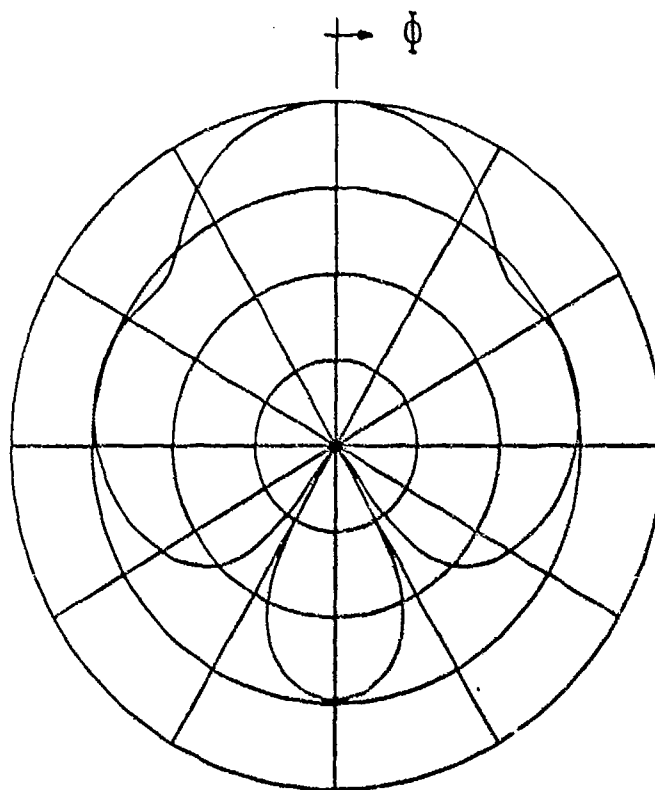
Figure 2.13: θ polarized near zone gain at $r = 5\lambda$ for the dipole array in the elevation plane.

4 ELEMENT DIPOLE ARRAY
FREQUENCY = 300.00 MHZ.
GAIN
POLARIZATION: θ
ELEV. PLANE: Φ =   0°   R= 10.000 M
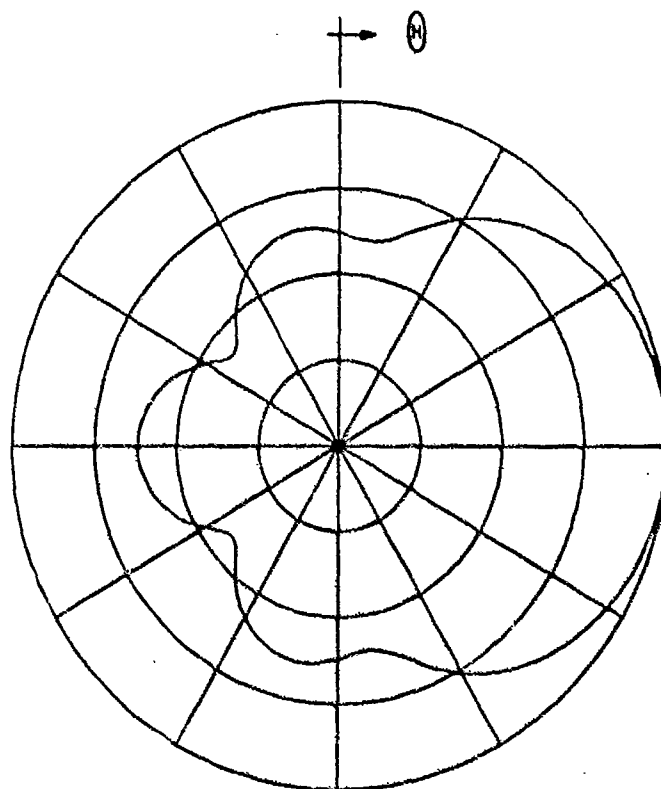MAXIMUM = 9.300 DB   10 DB/DIV.

Figure 2.14: θ polarized near zone gain at $r = 10\lambda$ for the dipole array in the elevation plane.

4 ELEMENT DIPOLE ARRAY
FREQUENCY = 300.00 MHZ.
GAIN
POLARIZATION: R
ELEV. PLANE: Φ = 0° R= 0.700 M
MAXIMUM = -6.400 DB   10 DB/DIV.

Figure 2.15: r̂ polarized near zone gain at $r = 0.7\lambda$ for the dipole array in the elevation plane.

21

```
4 ELEMENT DIPOLE ARRAY
FREQUENCY =  300.00 MHZ.
GAIN
POLARIZATION:  R
ELEV. PLANE: Φ =    0°    R=  1.000 M
MAXIMUM = -6.300 DB      10 DB/DIV.
```
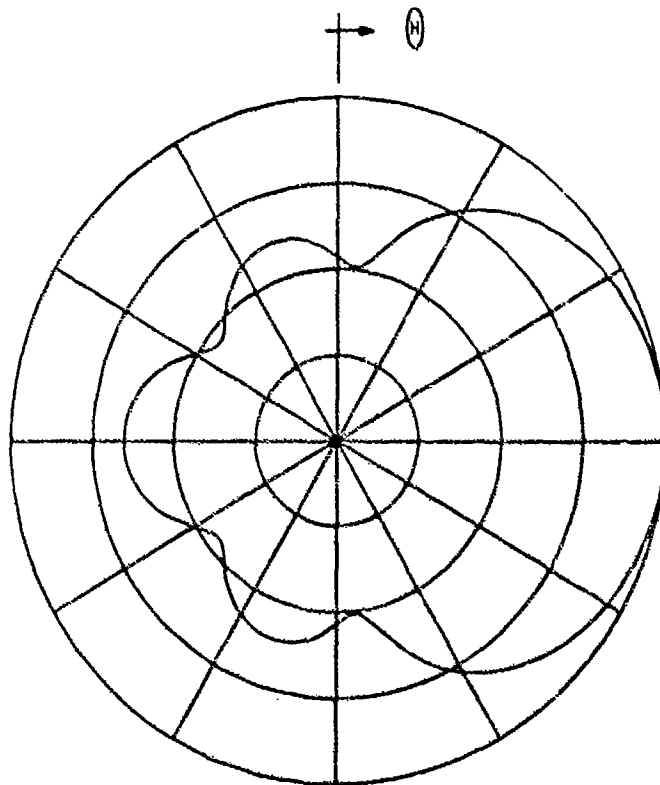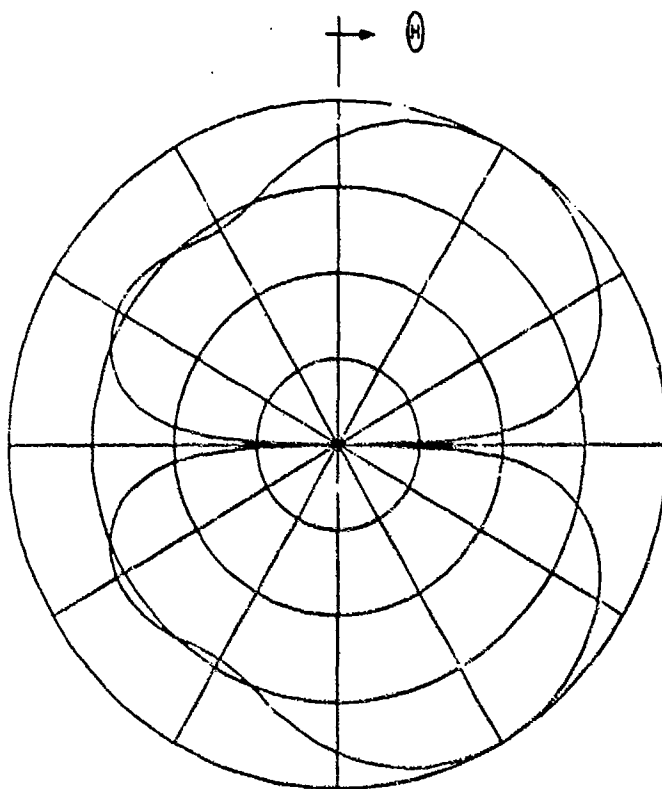
Figure 2.16: $\hat{r}$ polarized near zone gain at $r = 1\lambda$ for the dipole array in the elevation plane.

4 ELEMENT DIPOLE ARRAY
FREQUENCY = 300.00 MHZ.
GAIN
POLARIZATION: R
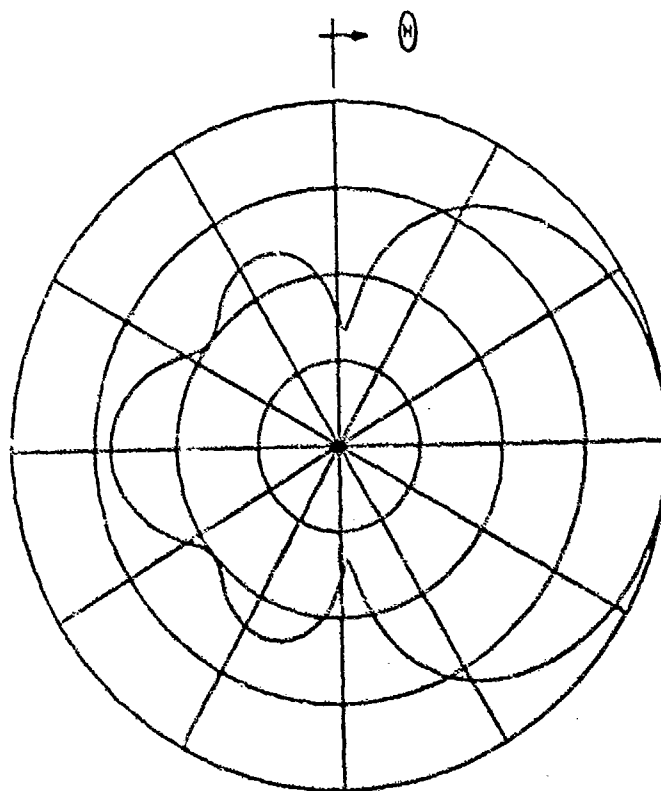ELEV. PLANE: Φ = 0° R= 2.000 M
MAXIMUM = -9.600 DB 10 DB/DIV.
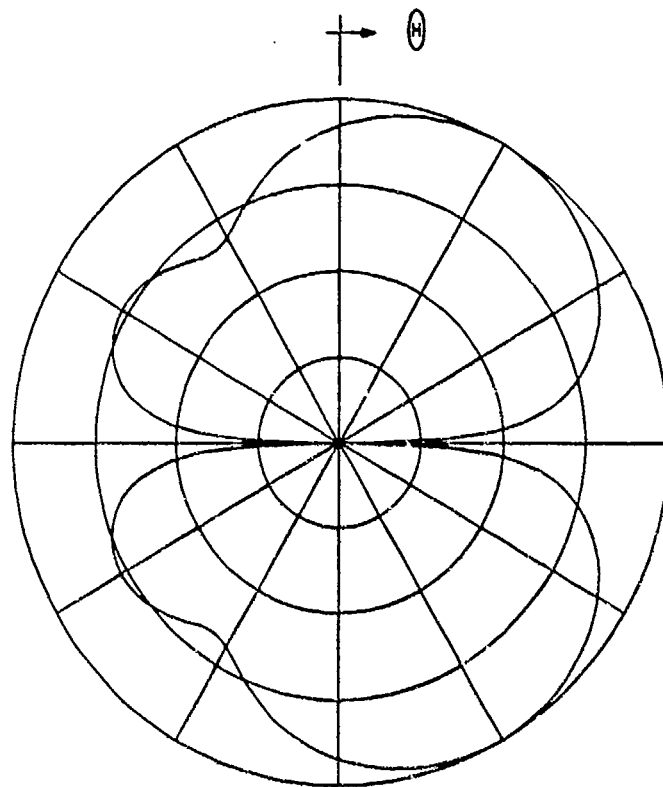
Figure 2.17: r̂ polarized near zone gain at $r = 2\lambda$ for the dipole array in the elevation plane.

23

4 ELEMENT DIPOLE ARRAY
FREQUENCY = 300.00 MHZ.
GAIN
POLARIZATION: R
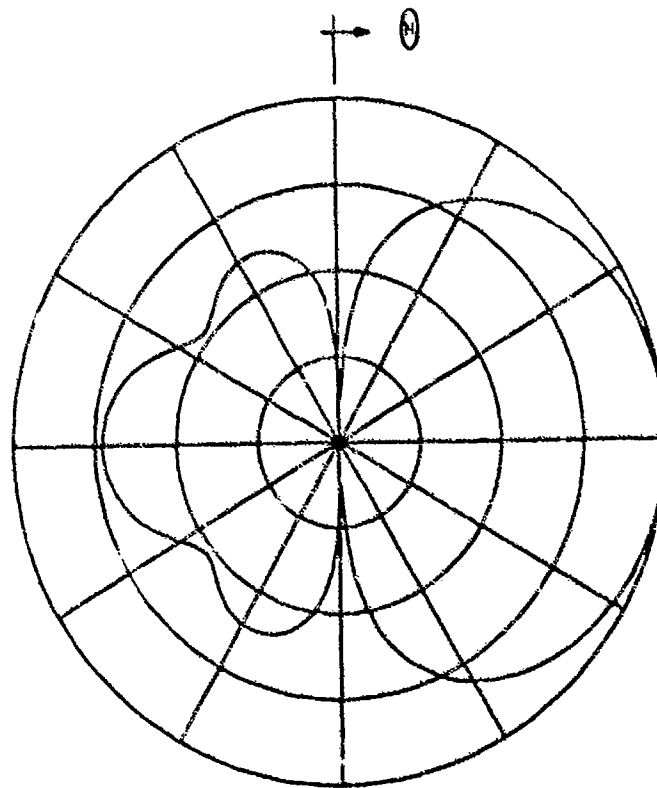ELEV. PLANE: Φ = 0° R= 5.000 M
MAXIMUM =-16.700 DB 10 DB/DIV.
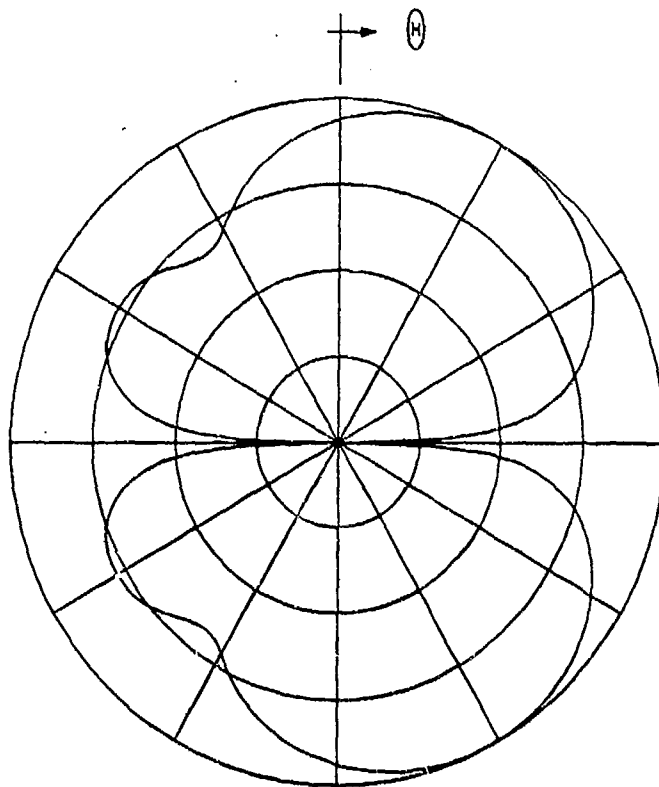
Figure 2.18: $\hat{r}$ polarized near zone gain at $r = 5\lambda$ for the dipole array in the elevation plane.

4 ELEMENT DIPOLE ARRAY
FREQUENCY = 300.00 MHZ.
GAIN
POLARIZATION: R
ELEV. PLANE: ϕ =   0°   R= 10.000 M
MAXIMUM =-22.600 DB   10 DB/DIV.

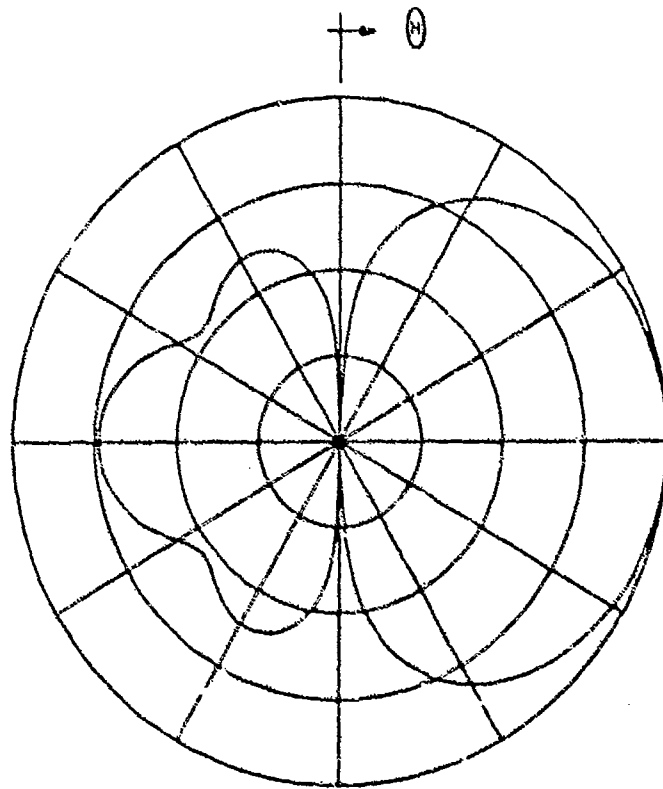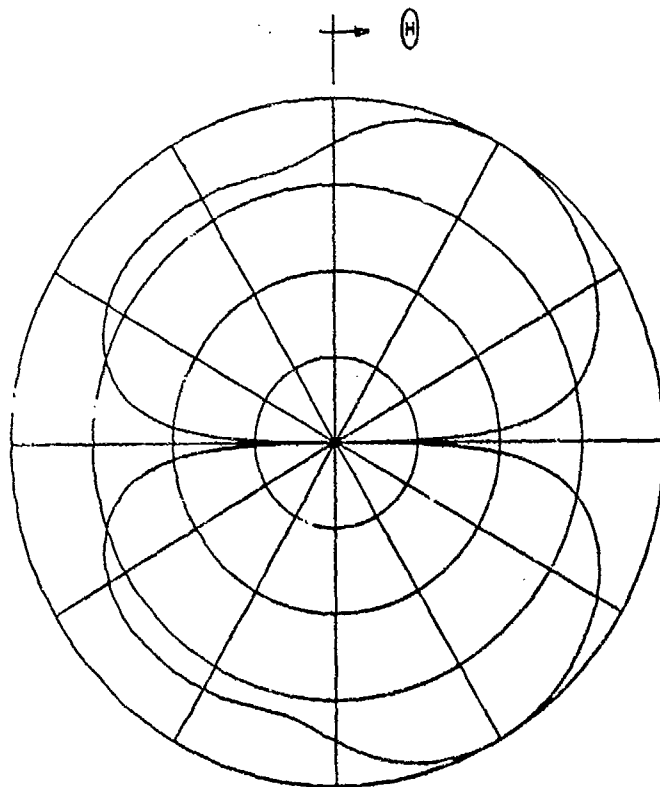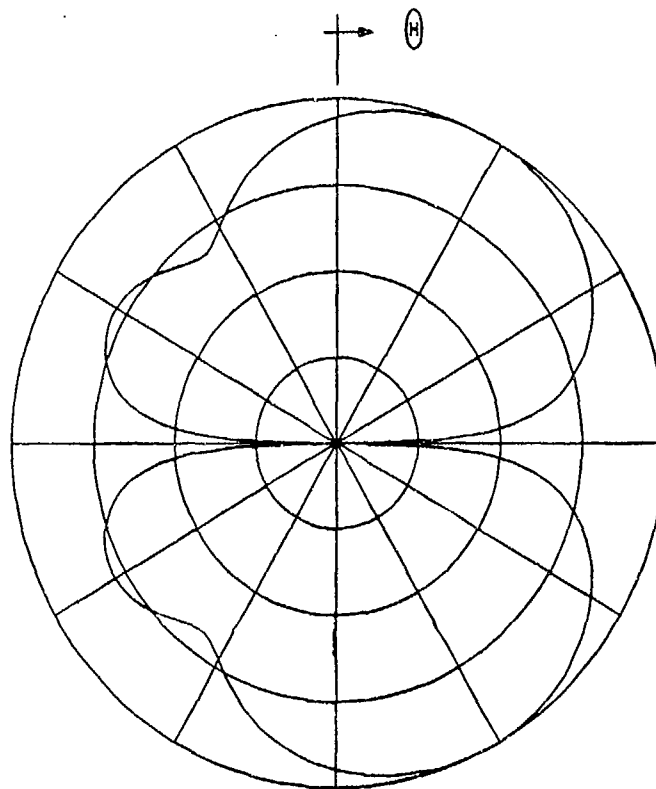Figure 2.19: $\hat{r}$ polarized near zone gain at $r = 10\lambda$ for the dipole array in the elevation plane.

4 ELEMENT DIPOLE ARRAY
FREQUENCY = 300.00 MHZ.
BACKSCATTER
POLARIZATION: θ-IN   θ-OUT
AZIM. PLANE: θ = 90°   R = ∞
MAXIMUM = 11.500 DB/M²   10 DB/DIV.
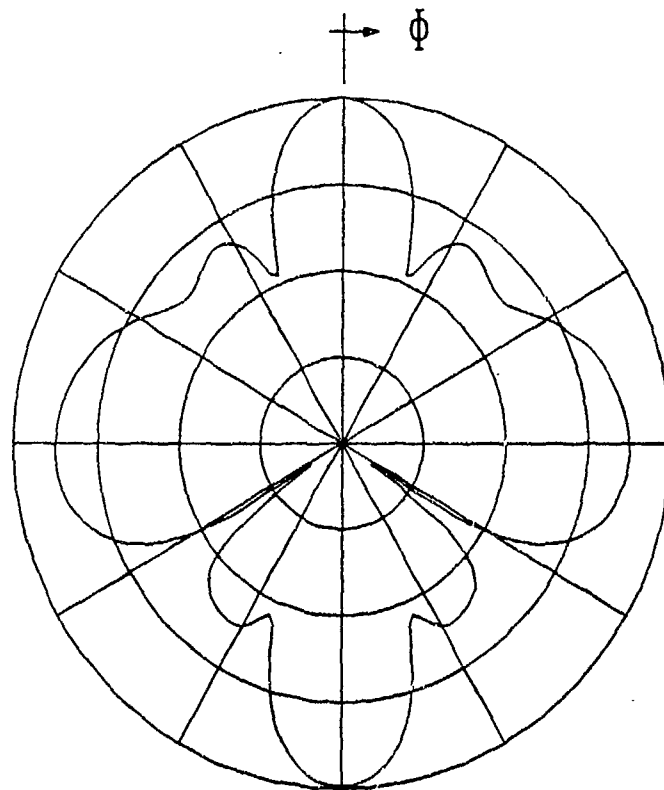
Figure 2.20: The $\hat{\theta}$ polarized far zone backscatter RCS for the dipole array in the azimuth plane.

4 ELEMENT DIPOLE ARRAY
FREQUENCY = 300.00 MHZ.
BACKSCATTER
POLARIZATION: θ-IN   θ-OUT
AZIM. PLANE: θ = 90°   R= 0.700 M
MAXIMUM = 9.500 DB/M^2 10 DB/DIV.

Figure 2.21: The $\hat{\theta}$ polarized near zone backscatter RCS for the dipole array at $r = 0.7\lambda$ in the azimuth plane.

27

4 ELEMENT DIPOLE ARRAY
FREQUENCY = 300.00 MHZ.
BACKSCATTER
POLARIZATION: θ-IN   θ-OUT
AZIM. PLANE: θ = 90°   R= 1.000 M
MAXIMUM = 10.600 DB/M^2 10 DB/DIV.

Figure 2.22: The $\hat{\theta}$ polarized near zone backscatter RCS for the dipole array at $r = \lambda$ in the azimuth plane.

28

4 ELEMENT DIPOLE ARRAY
FREQUENCY = 300.00 MHZ.
BACKSCATTER
POLARIZATION: Θ-IN   Θ-OUT
AZIM. PLANE: Θ = 90°   R= 2.000 M
MAXIMUM = 11.500 DB/M^2 10 DB/DIV.

Figure 2.23: The $\hat{\theta}$ polarized near zone backscatter RCS for the dipole array at $r = 2\lambda$ in the azimuth plane.

29

4 ELEMENT DIPOLE ARRAY
FREQUENCY = 300.00 MHZ.
BACKSCATTER
POLARIZATION: θ-IN   θ--OUT
AZIM. PLANE: θ =   90°   R= 5.000 M
MAXIMUM = 11.600 DB/M^2 10 DB/DIV.

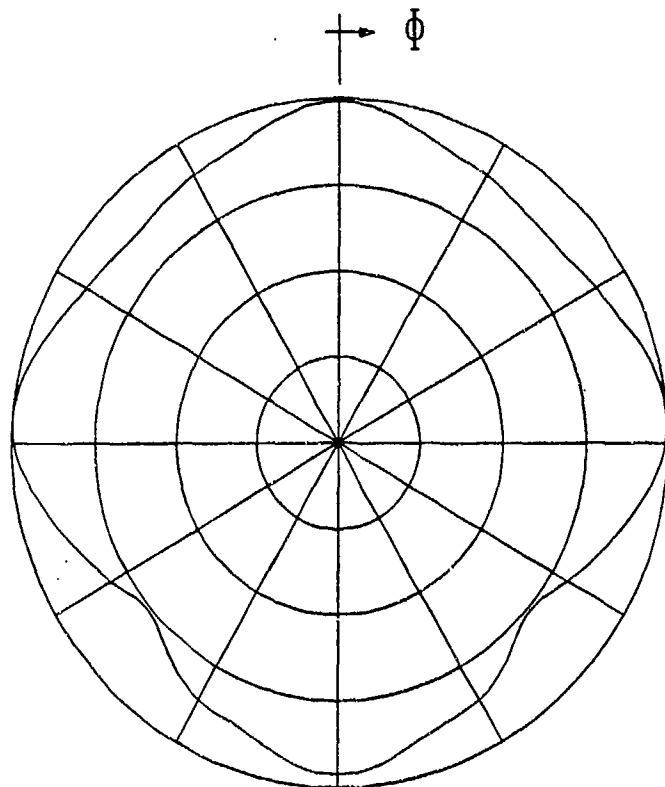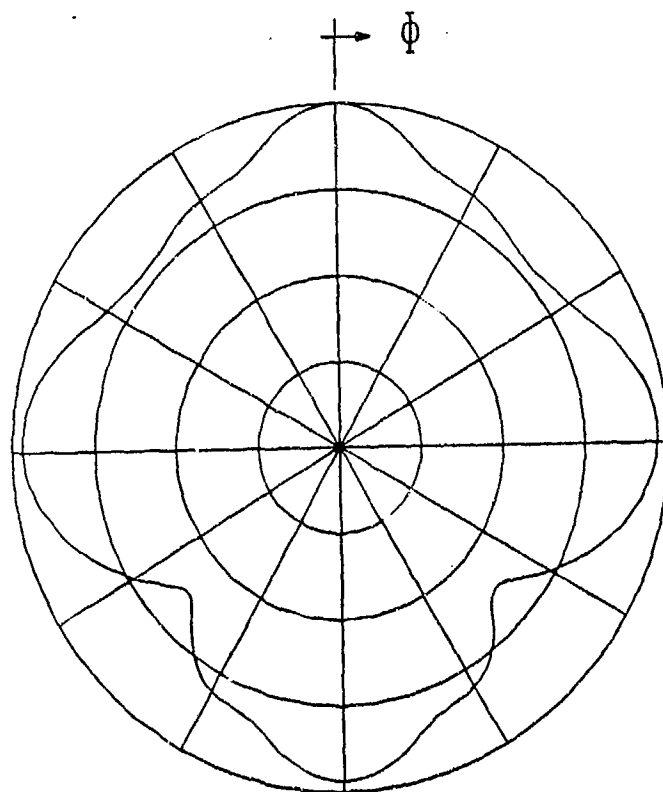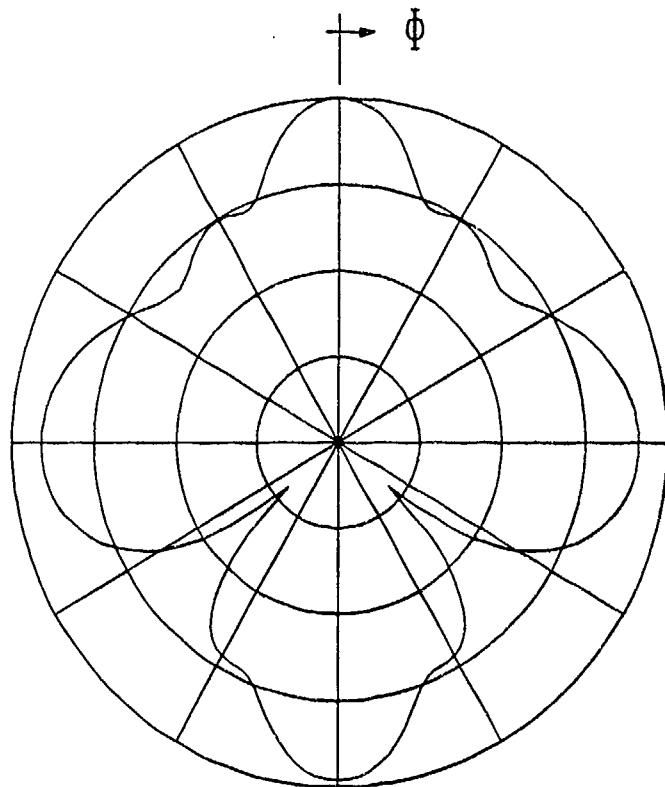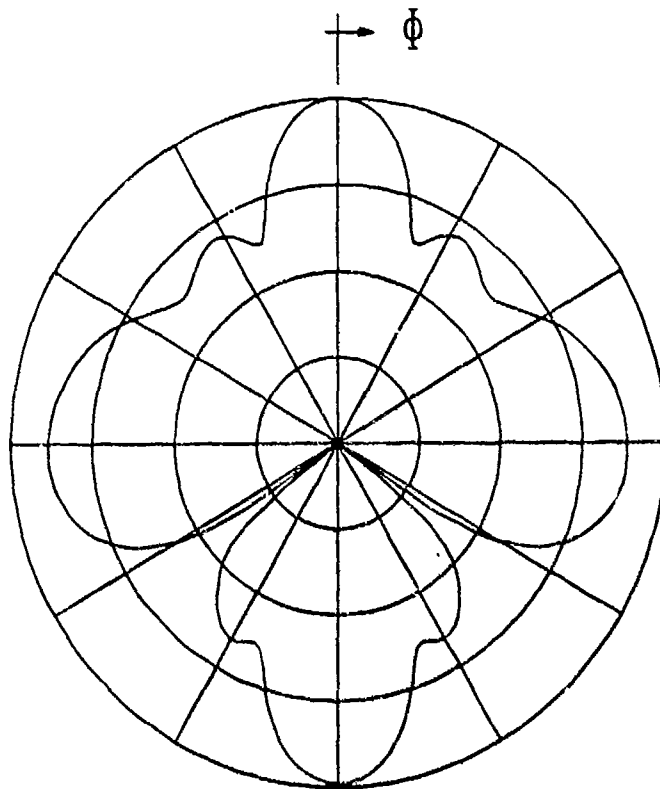Figure 2.24: The $\hat{\theta}$ polarized near zone backscatter RCS for the dipole array at $r = 5\lambda$ in the azimuth plane.

4 ELEMENT DIPOLE ARRAY
FREQUENCY = 300.00 MHZ.
BACKSCATTER
POLARIZATION: θ-IN θ-OUT
AZIM. PLANE: θ = 90°   R= 10.000 M
MAXIMUM = 11.600 DB/M^2 10 DB/DIV.
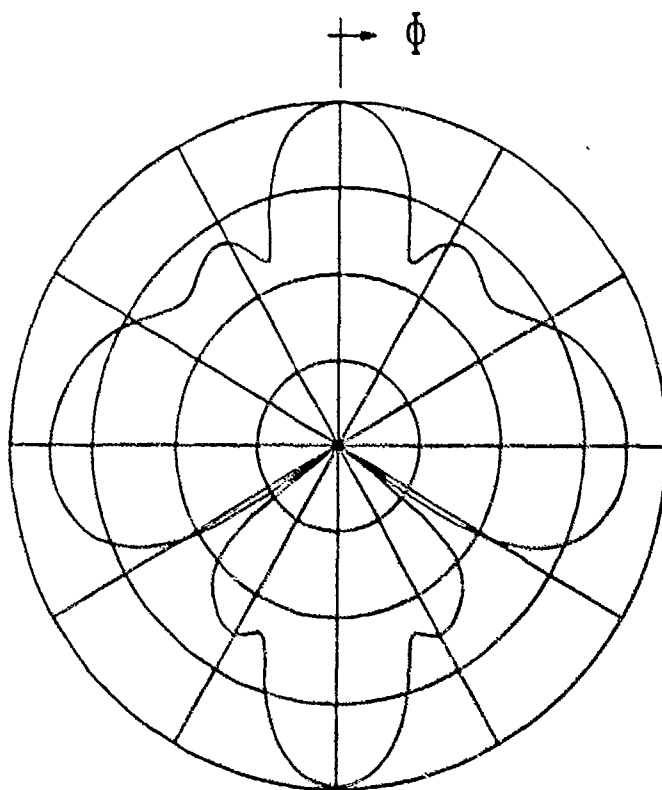
Figure 2.25: The $\hat{\theta}$ polarized near zone backscatter RCS for the dipole array at $r = 10\lambda$ in the azimuth plane.

31

$$\epsilon_0$$

$$\epsilon_r \ \epsilon_0 \qquad\qquad\qquad\qquad \updownarrow T$$

THIN DIELECTRIC PLATE
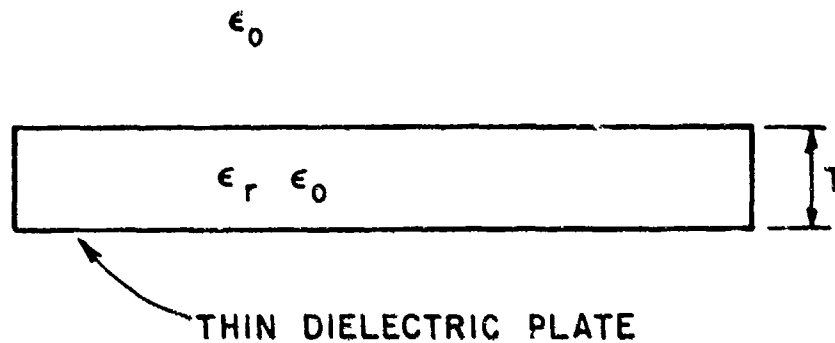
$$Z_s = \frac{1}{j\omega\epsilon_0(\epsilon_r-1)T}$$

Figure 2.26: Side view of a thin dielectric plate.

2.2 Thin Dielectric Plates

Previous versions of the ESP have been limited to treating plates of zero thickness and perfect conductivity. In this section we will describe the use of the sheet impedance approximation which will permit version IV of ESP to treat electrically thin dielectric plates.

Figure 2.26 shows the side view of a dielectric plate of thickness T and relative dielectric constant $\epsilon_r = \epsilon/\epsilon_0$ immersed in free space with permittivity $\epsilon_0 \approx 8.85 \times 10^{-12}$ F/m. If the slab is lossy, then ϵ_r will be complex. The sheet impedance approximation is valid provided:

1. The dielectric plate is sufficiently thin that the electric field is essentially uniform throughout its thickness. This will be the case provided $|k\sqrt{\epsilon_r}T| \ll 1$, where k is the free space wavenumber.

2. The dominant polarization of the electric field in the dielectric slab is parallel to the broad surfaces of the slab. This assumption is usually best satisfied when the incident field is polarized parallel to the broad surfaces of the slab or if $|\epsilon_r| \gg 1$.

If the above assumptions are satisfied, then the thin dielectric plate can be modeled as a zero thickness plate with sheet impedance [4]-[8]

$$Z_s = \frac{1}{j\omega\epsilon_0(\epsilon_r - 1)T} \quad \Omega. \tag{2.8}$$

The sheet impedance of a multilayer slab is simply the parallel combination of the sheet impedance of each layer [8]. For example, if we have a two layer slab, and if Z_{s1} and Z_{s2} denote the sheet impedance of the individual layers, then the sheet impedance of the two layer slab is

$$Z_s = \frac{Z_{s1}Z_{s2}}{Z_{s1} + Z_{s2}} \tag{2.9}$$

From Equation 2.8 it can be seen that if the dielectric slab is lossless, then Z_s is pure imaginary. If the slab is very lossy, such that $\text{Im}(\epsilon_r) \gg \text{Re}(\epsilon_r)$, then Equation 2.8 becomes

$$Z_s = \frac{1}{\sigma T} \quad \Omega, \tag{2.10}$$

where σ is the conductivity of the material. A material with pure real sheet impedance, as given by Equation 2.10, is referred to as a resistive sheet.

Probably the main advantage of the sheet impedance approximation is that it is relatively simple (as compared to more exact models) to implement. In particular, assume one has a surface patch MM computer code for perfectly conducting plates, such as the ESP code. Then to modify this code to treat plates with a sheet impedance, it is only necessary to add the term

$$\Delta Z_{mn} = \int\int_{m \to n} Z_s \mathbf{J}_m \cdot \mathbf{J}_n \, ds \tag{2.11}$$

to the mn term in the MM impedance matrix for the perfectly conducting plates. In Equation 2.11, $\mathbf{J}_m$ is the mth MM basis function, and the integration is over that portion of the surface where $\mathbf{J}_m$, $\mathbf{J}_n$, and Z_s are all non-zero. Note that the integration in Equation 2.11 is reasonably simple, even if Z_s varies over the surface. If $Z_s = 0$, then $\Delta Z_{mn} = 0$. A sheet impedance plate is thus a generalization of the perfectly conducting plate, with the perfectly conducting plate being the special case $Z_s = 0$. ESP Version IV has been set up to allow the user to specify a different Z_s for each plate. Thus, ESP IV will be able to treat combinations of perfectly

33

conducting and thin dielectric plates. Also, ESP IV will be able to compute the near or far zone fields of a surface impedance plate.

In our present implementation of the MM solution for a sheet impedance plate, we use the same current expansion or basis functions as for perfectly conducting plates. On a perfectly conducting plate the normal component of the surface current density goes to zero at the edges of the plate, and our basis functions enforce this condition. However, on a sheet impedance plate, the normal component of the surface current density need not vanish. Thus, the basis functions presently being used for sheet impedance plates are not optimum. The solution to this problem is to augment our present expansion modes with a series of edge modes which allow for a finite normal component of current at the edges of the sheet impedance plates. As described below, this has been done for a single plate (see Figures 2.36, 2.37 below), but a general technique not not been implemented in the ESP code.

The first example of the use of the sheet impedance model for a thin dielectric plate is shown in the insert in Figure 2.27. Here we have a 0.813 λ square dielectric plate of thickness $T = 0.051 \lambda$ and relative dielectric constant $\epsilon_r = 4$. Using Equation 2.8, this dielectric plate has a sheet impedance of $Z_s = -j392$ Ω. Figure 2.27 shows a comparison of the measured [9] and computed RCS in the elevation plane and for ϕ polarization. The same data is shown for the $\hat{\theta}$ polarization in Figure 2.28. Although there is overall agreement between computed and measured results in these figures, there are also noticeable differences. One reason for the differences is that for this dielectric plate

$$k\sqrt{\epsilon_r}T = 0.64$$

which is somewhat large to expect highly accurate results from the sheet impedance model. Also, for the $\hat{\theta}$ polarized RCS of Figure 2.28, near grazing incidence ($\theta_i = 0$, 180°) the incident field is polarized perpendicular to the broad surfaces of the plate. Thus, in this case the dominant electric field in the dielectric will be perpendicular to the broad surfaces of the slab. As described above, this violates the second condition for the sheet impedance approximation. We note that the presence of the electric field perpendicular to the broad surface of the dielectric plate can be accounted for by a magnetic sheet current, however, the complexity of the resulting solution is greatly increased [10].
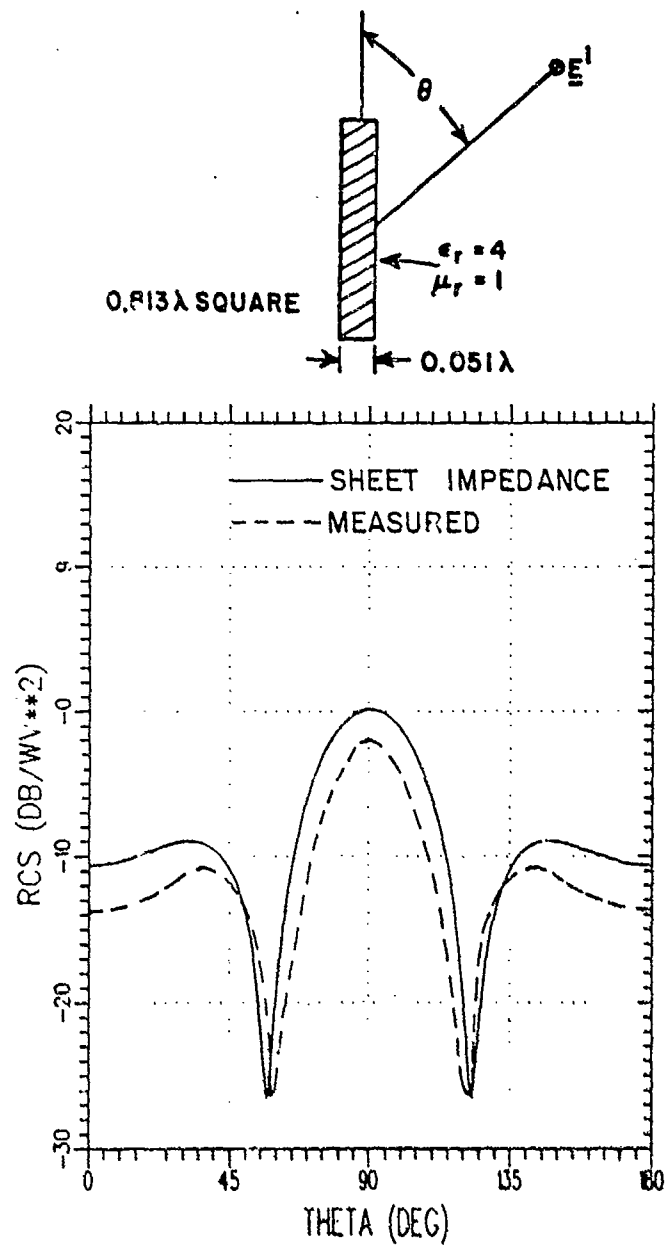
34

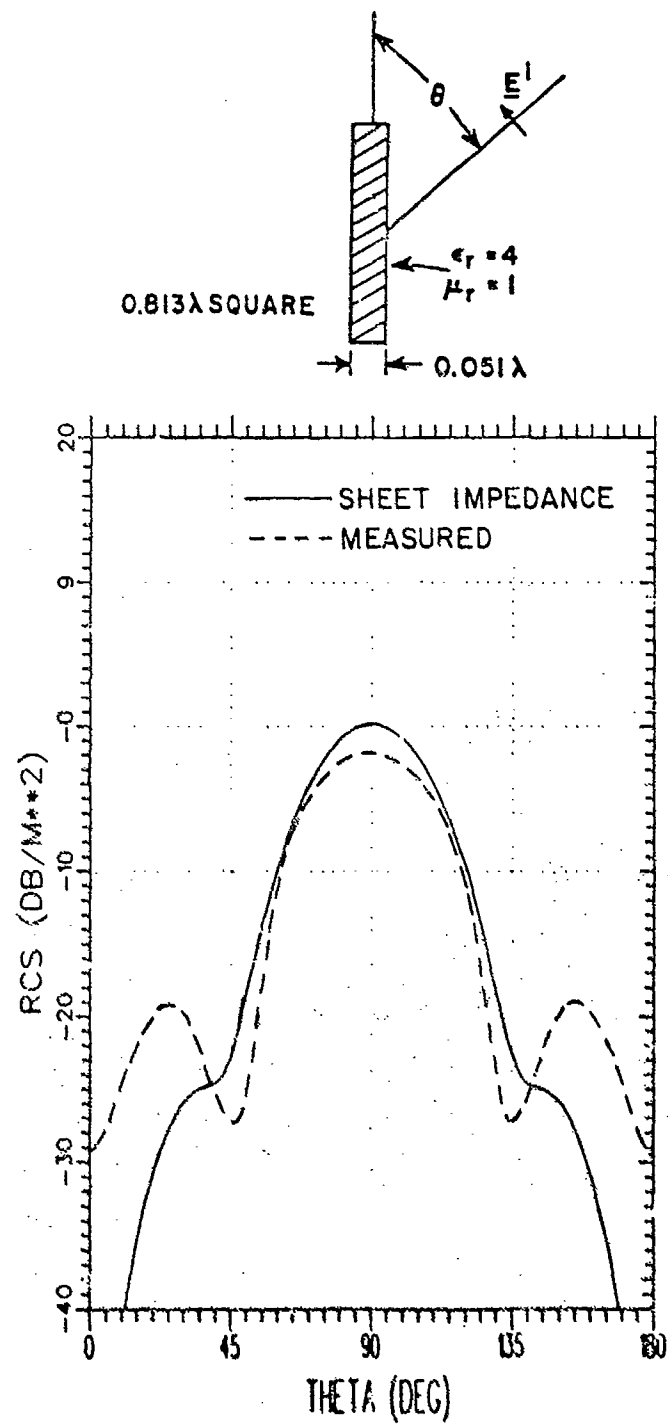Figure 2.27: The RCS of a 0.813 λ square dielectric plate at 300 Mhz. and for $\hat{\phi}$ polarization

35

Figure 2.28: The RCS of a 0.813 λ square dielectric plate at 300 Mhz. and for $\hat{\theta}$ polarization

36

The second example of the use of the sheet impedance model is illustrated in the insert in Figure 2.29. Here we have a dielectric cylindrical shell of height 3.73 cm, outer radius 1.27 cm, shell thickness $T = 0.254$ cm, and relative dielectric constant $\epsilon_r = 2.54$. Using Equation 2.8, at $f = 6.03$ Ghz this dielectric shell is equivalent to the sheet impedance $Z_s = -j763$ Ω. For the purpose of the MM model, the circular cylindrical dielectric shell is modelled by a zero thickness octagonal cylinder of radius 1.14 cm and surface impedance $-j763$ Ω. 56 surface patch modes are used to model the current on the cylinder.

Figures 2.29 and 2.30 show the dielectric cylinder elevation plane RCS patterns for the $\hat{\theta}$ and $\hat{\phi}$ polarizations. In these curves the solid line is measurements by Van Doeren [11], the dots are computations by Van Doeren, and the $\times'$ are our sheet impedance model computations. For this dielectric shell

$$k\sqrt{\epsilon_r}T = 0.32.$$

The agreement between our and Van Doeren's results is only fair.

As a final example, Figure 2.31 shows a dielectric strip of length 3.048 m, width 0.1829 m, and thickness $T = 0.0001829$ m, and with $\epsilon_r = 4$. The dielectric strip is excited by a unit amplitude $\hat{z}$ or $\hat{x}$ polarized plane wave incident from the $+y$ axis, i.e.,

$$E_z^i = E_x^i = e^{jky} \quad \text{V/m}.$$

At $f = 1$ GHz, this thin dielectric strip has the equivalent sheet impedance $Z_s = -j32800$ Ω. For a $\hat{z}$ polarized incident and scattered wave Figure 2.32 and 2.33 show the magnitude and phase of the near zone scattered electric field along the y axis (Note: $|E|$ in dB $= 20\log|E|$ in V/m). The solid line is a computation from Gupta [12] and the dashed line is the sheet impedance model. Figures 2.34 and 2.35 show the same data for the $\hat{x}$ polarization. In brief Gupta uses a volume polarization current model for the dielectric strip, and in this way is more exact than our sheet impedance model. However, he also uses asymptotic and far zone approximations in finding the fields of the currents, and in this way is less exact than our model. These Figures show almost perfect agreement for the $\hat{z}$ polarization, while the magnitude of the $\hat{x}$ polarized scattered field is about 1 to 2 dB below Gupta's computation.

The above three examples illustrate that our implementation of the sheet impedance model is capable of producing results within a few dB

Figure 2.29: The backscatter RCS of a dielectric cylindrical shell for $\hat{\theta}$ polarization of the incident electric field.

POLYSTYRENE TUBE
$\epsilon_r = 2.54 - j0.00$
FREQUENCY = 6.03 GHz
$Z_s = -j763\,\Omega$

x x x CALCULATED SHEET IMPEDANCE
• • • • CALCULATED VAN DOEREN
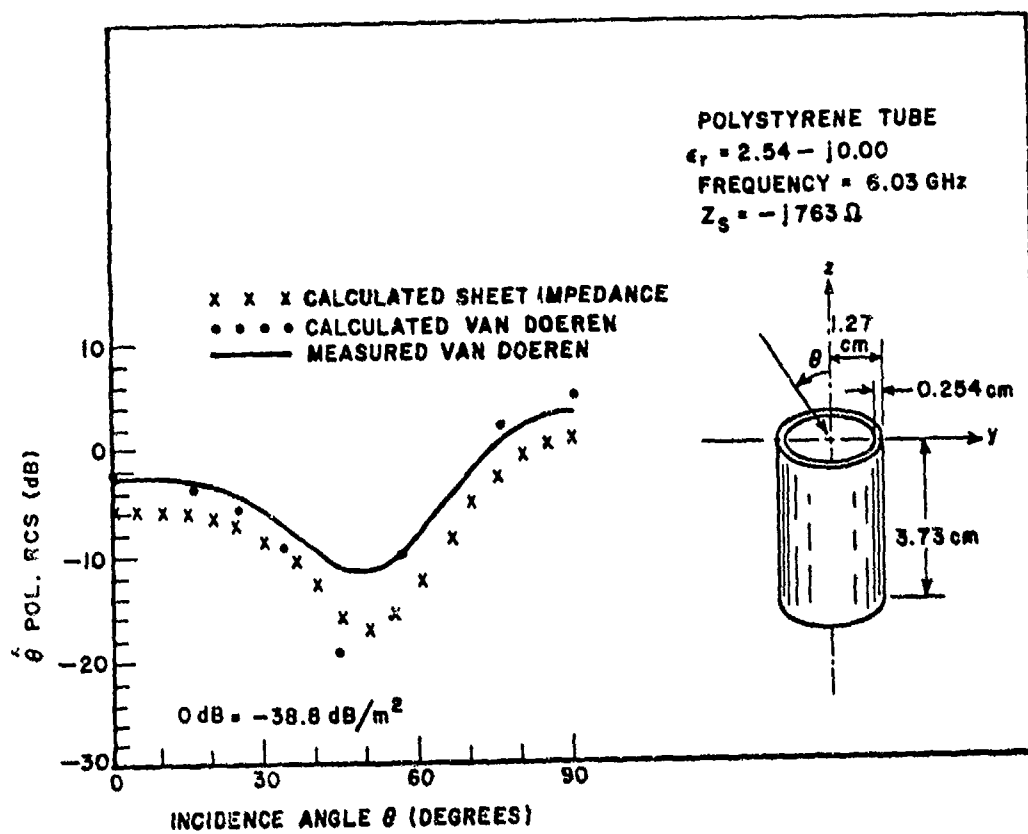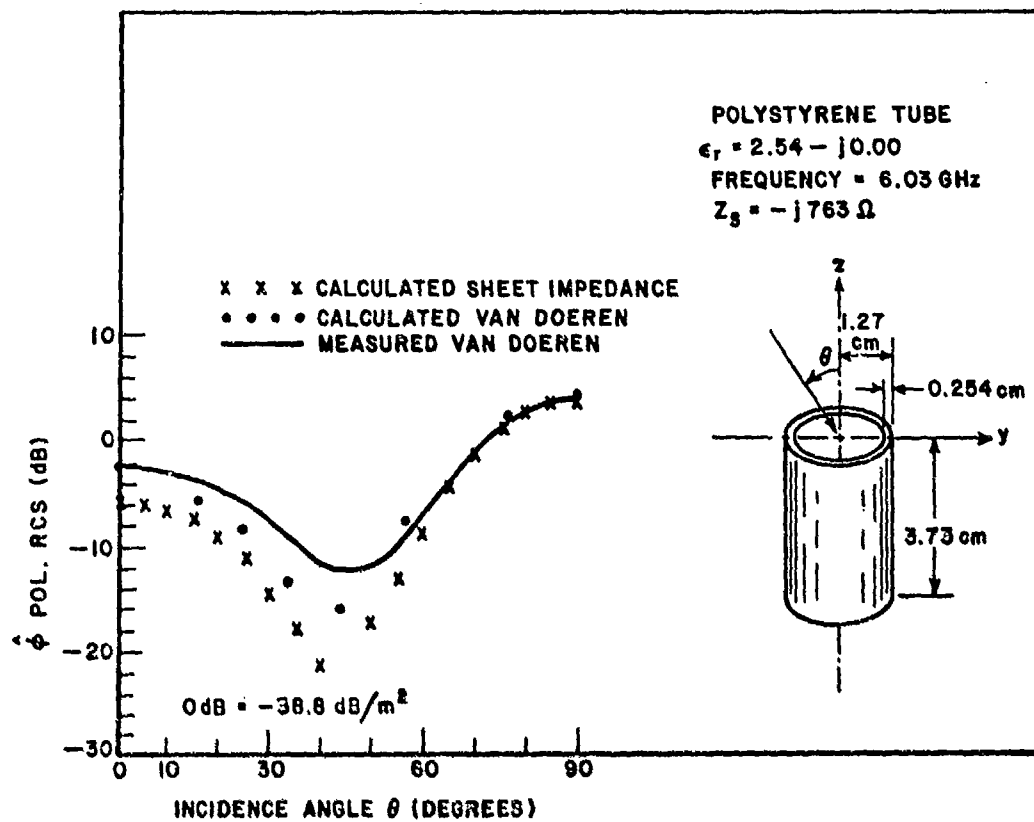——— MEASURED VAN DOEREN

0dB = −38.8 dB/m^2

Figure 2.30: The backscatter RCS of a dielectric cylindrical shell for $\hat{\phi}$ polarization of the incident electric field.
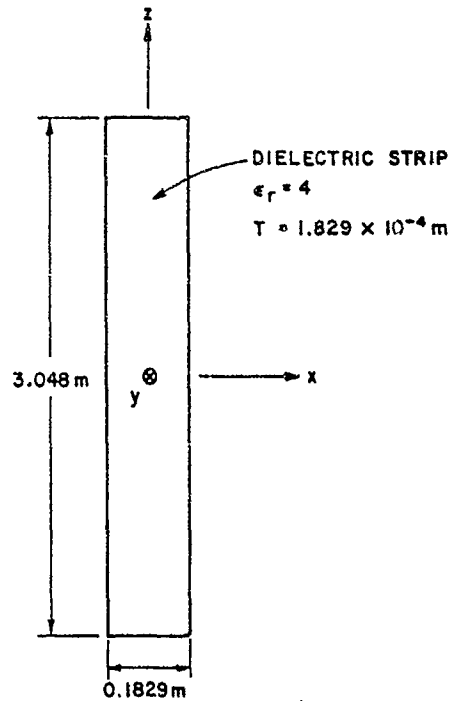
39

Figure 2.31: Side view of an electrically thin dielectric plate.

of the correct result. Although these results may be accurate enough for engineering accuracy, some improvement is possible. In particular consider Figure 2.34, where our results are a couple of dB below Gupta's computations. For this dielectric strip

$$k\sqrt{\epsilon_r}T = 0.0011,$$

and the incident field is polarized parallel to the broad face of the strip. Thus we would expect the sheet impedance approximation to be very accurate, and would not expect the 2 dB difference evident in Figure 2.34. Thus, as described above, we expect that a substantial portion of the error in Figure 2.34 is due to the fact that our expansion for the surface current density on the sheet impedance plates vanishes at the edges, while the actual current does not. To test this hypothesis, we added a series of edge modes which allowed for finite surface current density at the edge of the sheet impedance plate. Figures 2.36,2.37 repeat the same data as in Figures 2.34,2.35, except the computation included these edge modes. Comparing Figures 2.34 and 2.36 shows that adding the edge modes considerably improved the agreement between our and Gupta's results.

In summary we have implemented in the ESP code a simple sheet for

40

thin dielectric plates. The simple sheet impedance model is capable of predicting near or far zone fields to within a few dB of the actual values. The accuracy of our model could be improved through the addition of the above described edge modes.
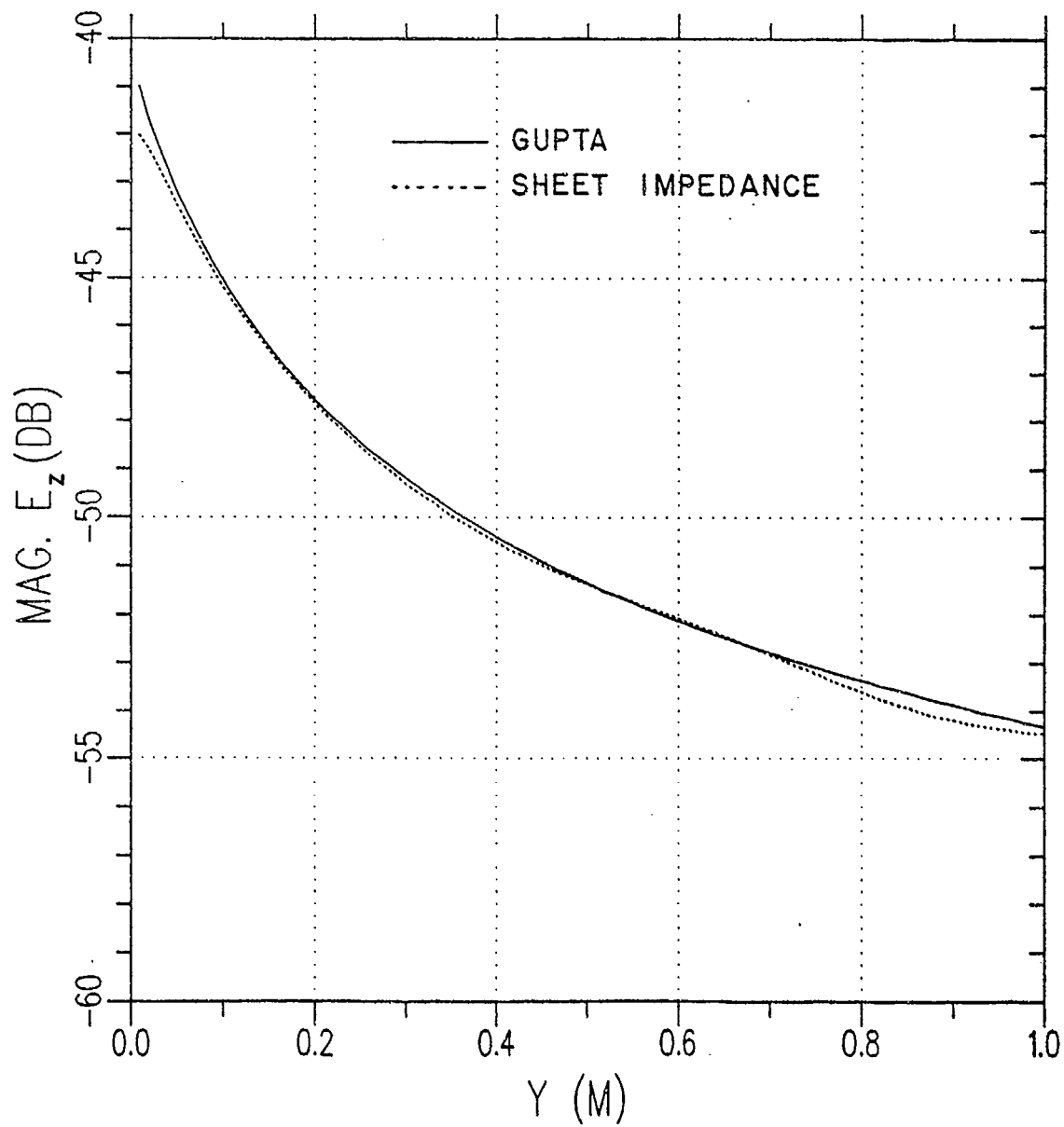
Figure 2.32: The magnitude (V/m) of the near zone E_z field, on the line $(x = 0, y, z = 0)$, for the dielectric strip of Figure 2.31 caused by a normally incident $\hat{z}$ polarized plane wave.

Figure 2.33: The phase of the near zone E_z field, on the line $(x = 0, y, z = 0)$, for the dielectric strip of Figure 2.31 caused by a normally incident $\hat{z}$ polarized plane wave.

43

Figure 2.34: The magnitude (V/m) of the near zone E_x field, on the line $(x = 0, y, z = 0)$, for the dielectric strip of Figure 2.31 caused by a normally incident $\hat{x}$ polarized plane wave.
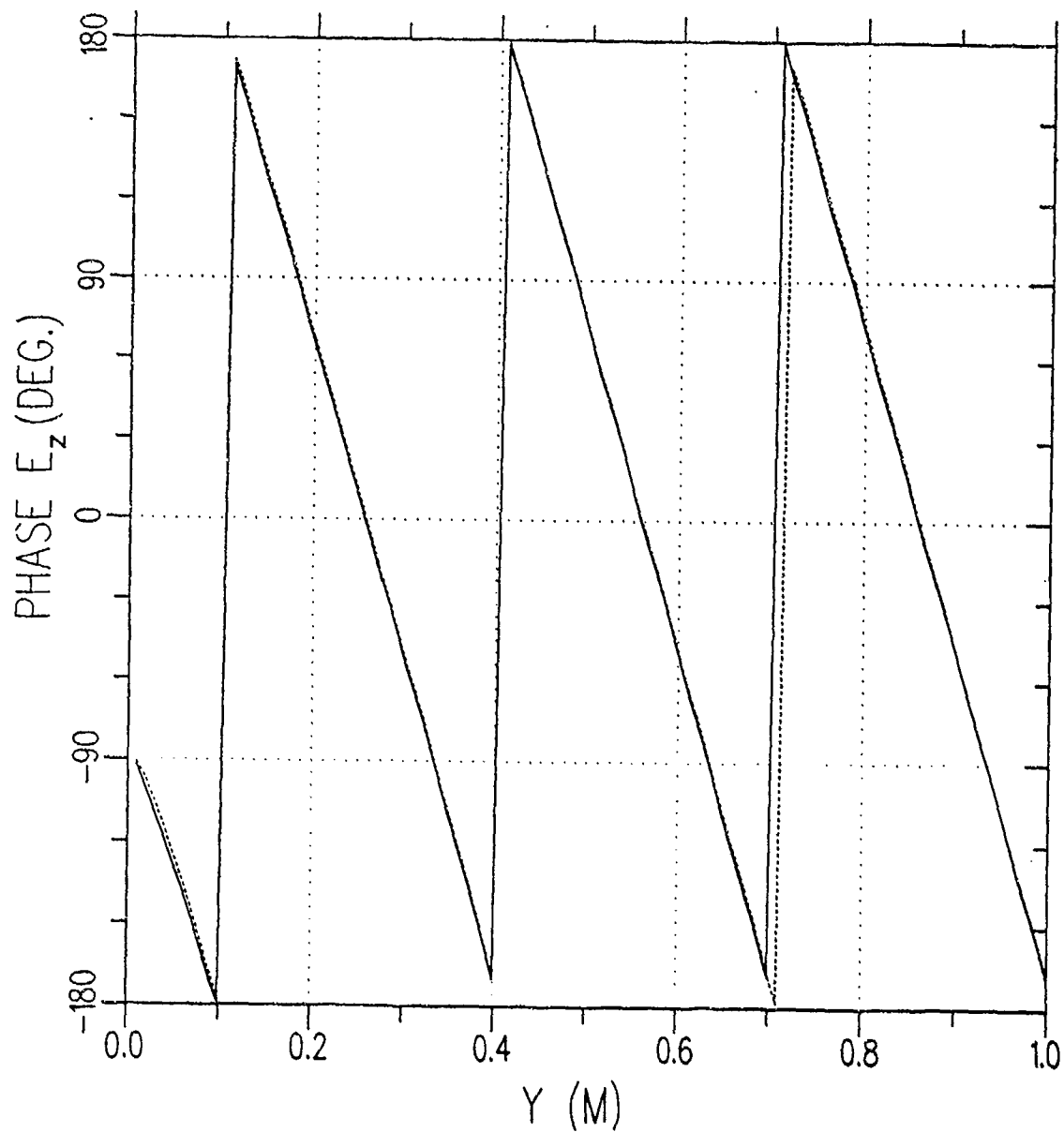
44

Figure 2.35: The phase of the near zone E_x field, on the line $(x = 0, y, z = 0)$, for the dielectric strip of Figure 2.31 caused by a normally incident $\hat{x}$ polarized plane wave.
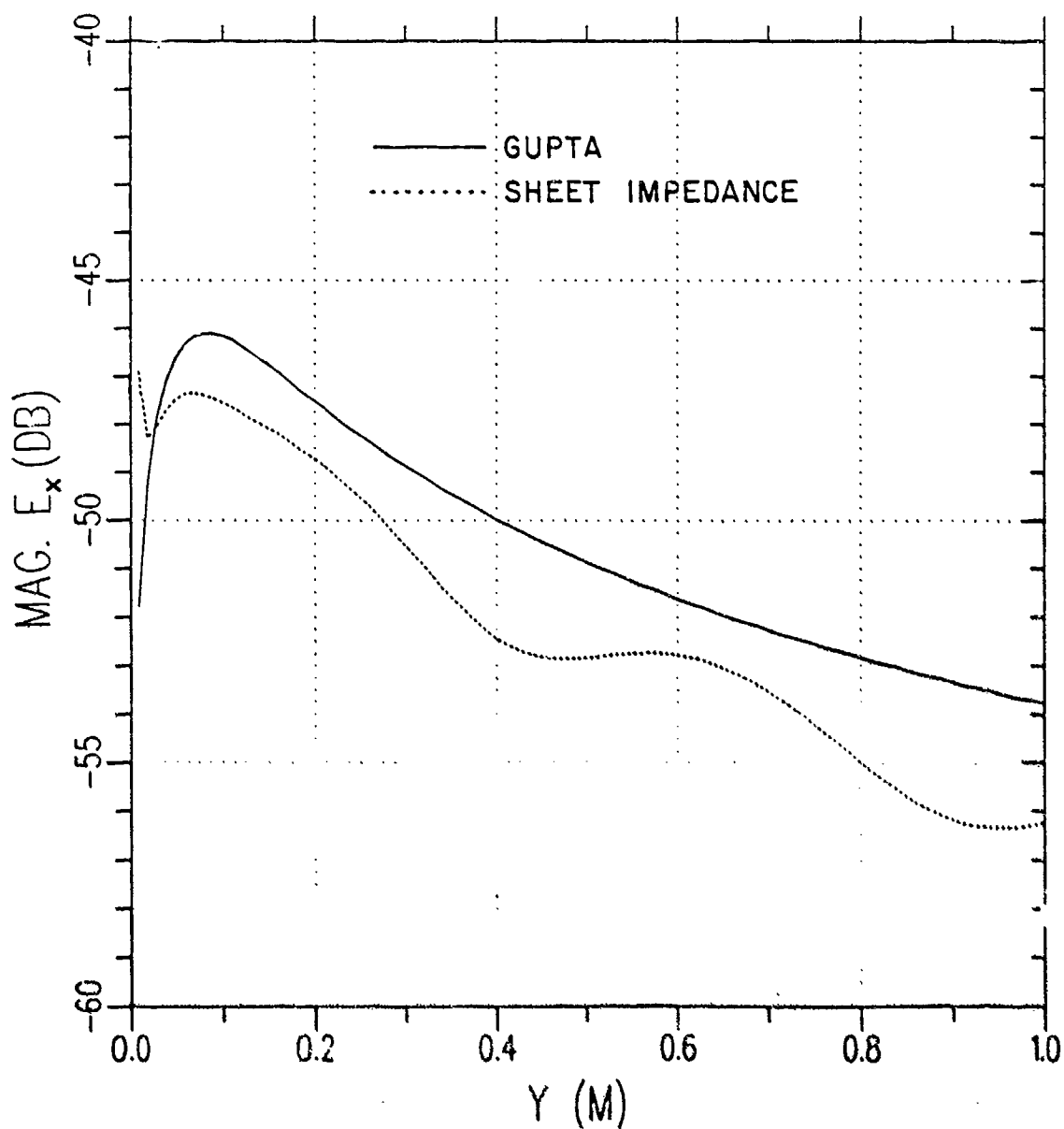
Figure 2.36: The magnitude (V/m) of the near zone E_x field, on the line $(x = 0, y, z = 0)$, for the dielectric strip of Figure 2.31 caused by a normally incident $\hat{z}$ polarized plane wave. Data computed with edge modes.
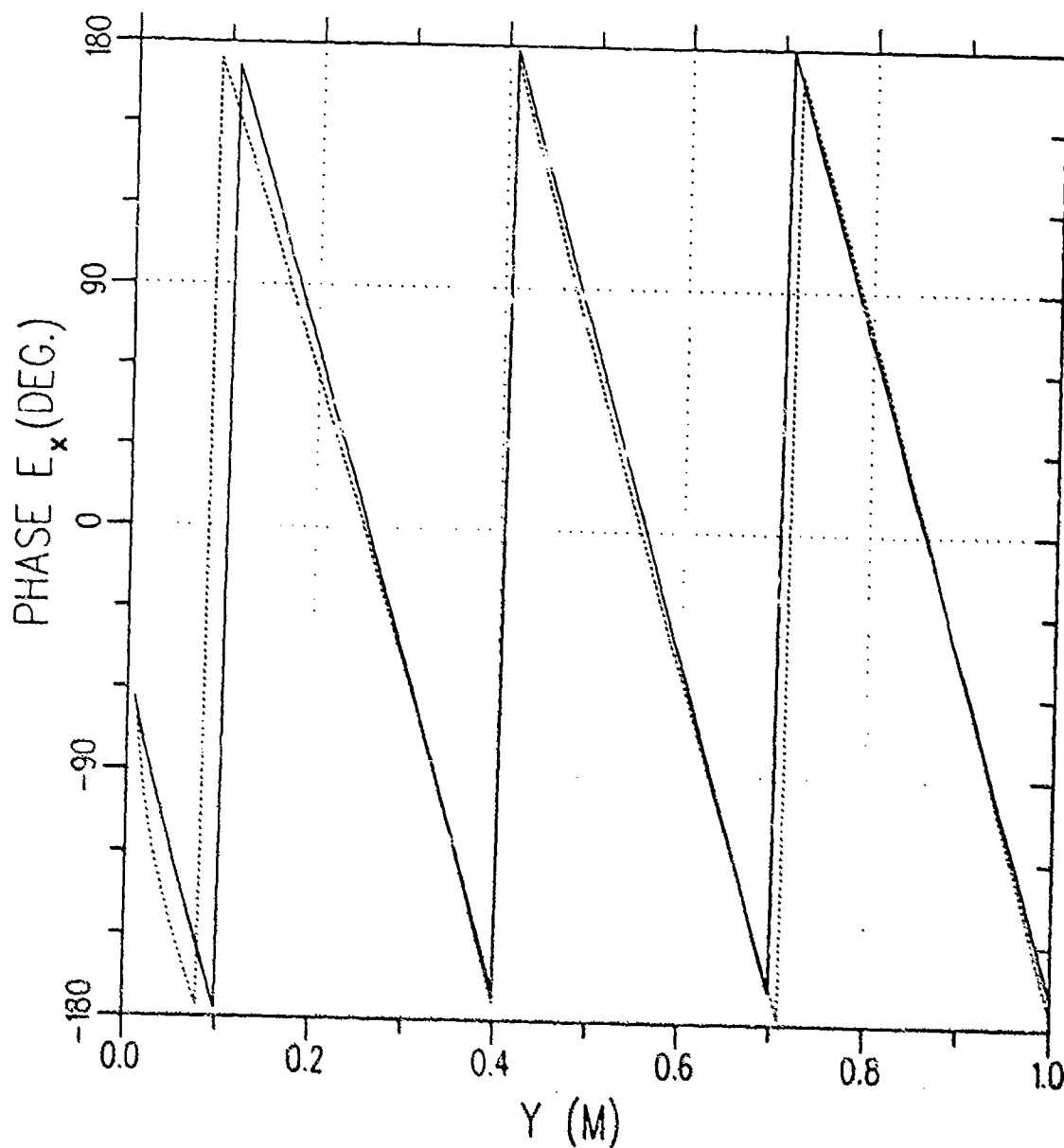
46

Figure 2.37: The phase of the near zone E_x field, on the line $(x = 0, y = 0)$, for the dielectric strip of Figure 2.31 caused by a normally incident $\hat{z}$ polarized plane wave. Data computed with edge modes.
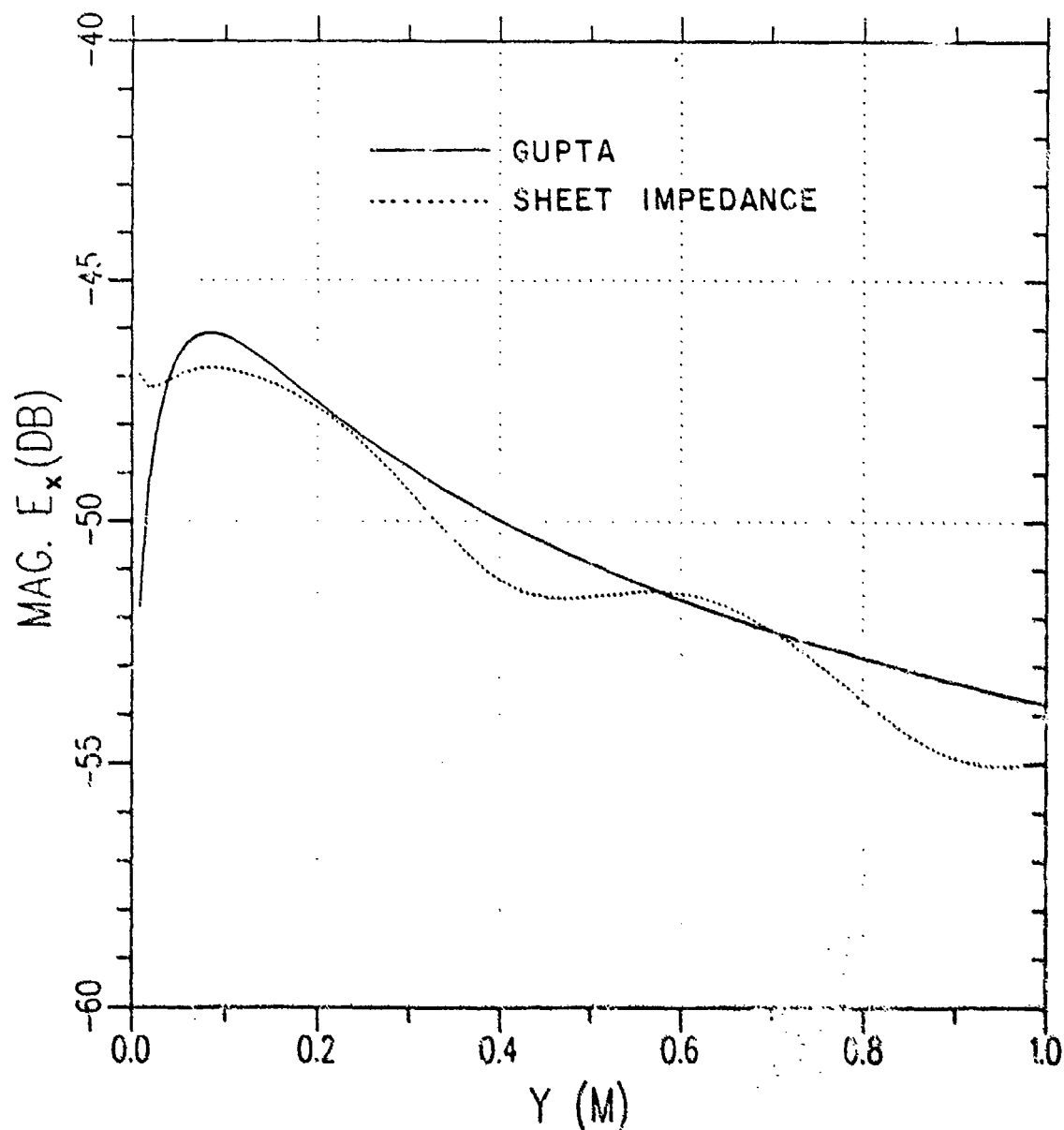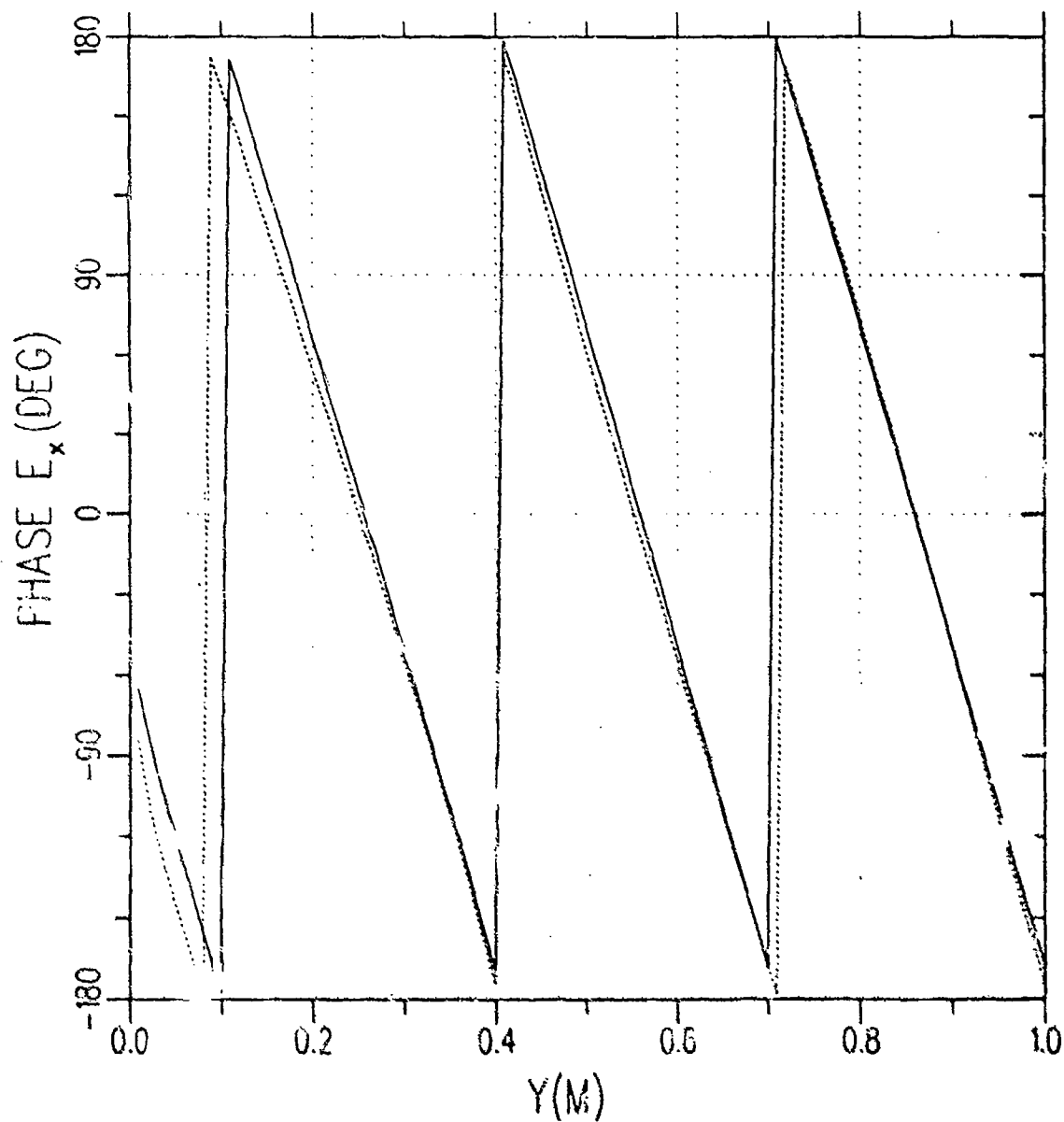
47

Chapter 3

Summary

This report has described two recent modifications to the ESP code. ESP is a user oriented code for the analysis of the electromagnetic radiation and scattering from geometries consisting of interconnections of thin wires and plates. The two modifications or improvements are:

1. the ability to compute near zone radiation and scatter.ng patterns (previously ESP could only compute far zone patterns),

2. the ability to analyze thin dielectric plates through a shee: impedance model (previously ESP could only analyze perfectly conducting plates).

These two features should be part of the next version (IV) of the ESP code.

Bibliography

[1] R.F. Harrington, *Field Computations by Moment Methods* New York, Macmillan, 1968.

[2] E.H. Newman and R.L. Dilsavor, "A User's Manual for the Electromagnetic Surface Patch Code: ESP Version III", Technical Report 716148-19, prepared under Grant NSG 1613, between the Ohio State University Research Foundation and the National Aeronautics and Space Administration, Langley Research Center, Hampton, VA 22217, May 1987.

[3] E.H. Newman, "Generation of Wideband Data from the Method of Moments by Interpolating the Impedance Matrix", IEEE Trans. on Antennas and Propagation, submitted for publication.

[4] R.F. Harrington and J.R. Mautz, "An Impedance Sheet Approximation for Thin Dielectric Shells", IEEE Trans. on Antennas and Propagation, Vol. AP-23, pp. 531-534, July 1975.

[5] T.B.A. Senior, "Backscattering from Resistive Strips", IEEE Trans. on Antennas and Propagation, Vol. AP-27, pp. 808-813, Nov. 1979.

[6] M.G. Andreason, "Back-Scattering Cross Section of a Thin, Dielectric, Spherical Shell", IEEE Trans. on Antennas and Propagation, Vol. AP-5, pp. 267-270, July 1975.

[7] E.H. Newman and M.R. Schrote, "An Open Surface Integral Formulation for Electromagnetic Scattering by Material Plates", IEEE Trans. on Antennas and Propagation, Vol. AP-32, pp. 672-678, July 1984.

[8] E.H. Newman and and J.L. Blanchard, "TM Scattering by an Impedance Sheet Extension of a Parabolic Cylinder", IEEE Trans. on Antennas and Propagation, accepted for publication.

[9] H.L. Thal and J.F. Finger, "Scattering by Dielectric Containers", IEEE Trans. on Antennas and Propagation, Vol. AP-18, pp. 709-711, September 1970.

[10] Thomas B.A. Senior and John L. Volakis, "Sheet Simulation of a Thin Dielectric Layer", submitted for publication to Radio Science.

[11] R.E. Van Doeren, "Arbitrary Incidence Backscattering from Thin-Wall Dielectric Tubes Having Finite Length", Ohio State Univ. Research Foundation Report 2767-1, prepared under contract N00019-69-C-0325 with the Dept. of the Navy, Naval Air Systems Command, August 1, 1969.

[12] I.J. Gupta, Ohio State University ElectroScience Lab, private communication.

MISSION
of
Rome Air Development Center

RADC plans and executes research, development, test and selected acquisition programs in support of Command, Control, Communications and Intelligence (C^3I) activities. Technical and engineering support within areas of competence is provided to ESD Program Offices (POs) and other ESD elements to perform effective acquisition of C^3I systems. The areas of technical competence include communications, command and control, battle management information processing, surveillance sensors, intelligence data collection and handling, solid state sciences, electromagnetics, and propagation, and electronic reliability/maintainability and compatibility.